

The CARMENES search for exoplanets around M dwarfs

Planet occurrence rates from a subsample of 71 stars

S. Sabotta^{1,2}, M. Schlecker³, P. Chaturvedi¹, E. W. Guenther¹, I. Muñoz Rodríguez⁴, J. C. Muñoz Sánchez^{5,6}, J. A. Caballero⁷, Y. Shan⁸, S. Reffert², I. Ribas^{5,6}, A. Reiners⁸, A. P. Hatzes¹, P. J. Amado⁴, H. Klahr³, J. C. Morales^{5,6}, A. Quirrenbach², Th. Henning³, S. Dreizler⁸, E. Pallé^{9,10}, M. Perger^{5,6}, M. Azzaro¹¹, S. V. Jeffers¹², A. Kaminski², M. Kürster³, M. Lafarga^{5,6,13}, D. Montes¹⁴, V. M. Passegger^{15,16}, and M. Zechmeister⁸

¹ Thüringer Landessternwarte Tautenburg, Sternwarte 5, 07778 Tautenburg, Germany

² Landessternwarte, Zentrum für Astronomie der Universität Heidelberg, Königstuhl 12, 69117 Heidelberg, Germany
e-mail: silvia.sabotta@lsw.uni-heidelberg.de

³ Max-Planck-Institut für Astronomie, Königstuhl 17, 69117 Heidelberg, Germany

⁴ Instituto de Astrofísica de Andalucía (IAA-CSIC), Glorieta de la Astronomía s/n, 18008 Granada, Spain

⁵ Institut de Ciències de l'Espai (ICE, CSIC), Campus UAB, c/ de Can Magrans s/n, 08193 Cerdanyola del Vallès, Barcelona, Spain

⁶ Institut d'Estudis Espacials de Catalunya (IEEC), c/ Gran Capità 2-4, 08034 Barcelona, Spain

⁷ Centro de Astrobiología (CSIC-INTA), ESAC, Camino bajo del castillo s/n, 28692 Villanueva de la Cañada, Madrid, Spain

⁸ Institut für Astrophysik, Georg-August-Universität, Friedrich-Hund-Platz 1, 37077 Göttingen, Germany

⁹ Instituto de Astrofísica de Canarias, Vía Láctea s/n, 38205 La Laguna, Tenerife, Spain

¹⁰ Departamento de Astrofísica, Universidad de La Laguna, 38026 La Laguna, Tenerife, Spain

¹¹ Max-Planck Institute for Solar System Research Justus-von-Liebig Weg 3, 37077 Goettingen, Germany

¹² Centro Astronómico Hispano-Alemán (CSIC-Junta de Andalucía), Observatorio Astronómico de Calar Alto, Sierra de los Filabres, 04550 Gérgal, Almería, Spain

¹³ Department of Physics, University of Warwick, Gibbet Hill Road, Coventry CV4 7AL, UK

¹⁴ Departamento de Física de la Tierra y Astrofísica & IPARCOS-UCM (Instituto de Física de Partículas y del Cosmos de la UCM), Facultad de Ciencias Físicas, Universidad Complutense de Madrid, 28040 Madrid, Spain

¹⁵ Hamburger Sternwarte, Gojenbergsweg 112, 21029 Hamburg, Germany

¹⁶ Homer L. Dodge Department of Physics and Astronomy, University of Oklahoma, 440 West Brooks Street, Norman, OK 73019, USA

Received 31 March 2021 / Accepted 29 June 2021

ABSTRACT

Context. The CARMENES exoplanet survey of M dwarfs has obtained more than 18 000 spectra of 329 nearby M dwarfs over the past five years as part of its guaranteed time observations (GTO) program.

Aims. We determine planet occurrence rates with the 71 stars from the GTO program for which we have more than 50 observations.

Methods. We use injection-and-retrieval experiments on the radial-velocity time series to measure detection probabilities. We include 27 planets in 21 planetary systems in our analysis.

Results. We find $0.06^{+0.04}_{-0.03}$ giant planets ($100 M_{\oplus} < M_{\text{pl}} \sin i < 1000 M_{\oplus}$) per star in periods of up to 1000 d, but due to a selection bias this number could be up to a factor of five lower in the whole 329-star sample. The upper limit for hot Jupiters (orbital period of less than 10 d) is 0.03 planets per star, while the occurrence rate of planets with intermediate masses ($10 M_{\oplus} < M_{\text{pl}} \sin i < 100 M_{\oplus}$) is $0.18^{+0.07}_{-0.05}$ planets per star. Less massive planets with $1 M_{\oplus} < M_{\text{pl}} \sin i < 10 M_{\oplus}$ are very abundant, with an estimated rate of $1.32^{+0.33}_{-0.31}$ planets per star for periods of up to 100 d. When considering only late M dwarfs with masses $M_{\star} < 0.34 M_{\odot}$, planets more massive than $10 M_{\oplus}$ become rare. Instead, low-mass planets with periods shorter than 10 d are significantly overabundant.

Conclusions. For orbital periods shorter than 100 d, our results confirm the known stellar mass dependences from the *Kepler* survey: M dwarfs host fewer giant planets and at least two times more planets with $M_{\text{pl}} \sin i < 10 M_{\oplus}$ than G-type stars. In contrast to previous results, planets around our sample of very low-mass stars have a higher occurrence rate in short-period orbits of less than 10 d. Our results demonstrate the need to take into account host star masses in planet formation models.

Key words. planetary systems – techniques: radial velocities – methods: data analysis – stars: low-mass

1. Introduction

An open question in exoplanet research is if planet formation theories produce the same exoplanet population as the observed one. In order to answer this question, it is crucial to study the population of planets as a function of stellar mass. We expect the

planet occurrence rate to change with the mass of the host star because more massive stars host more massive protoplanetary disks (Mordasini et al. 2012a; Andrews et al. 2013; Pascucci et al. 2016; Ansdell et al. 2016; Tychoniec et al. 2018).

Exoplanet surveys of low-mass M dwarfs are very important because they investigate the most abundant type of star

(Henry et al. 2006, 2018; Reylé et al. 2021). They have the potential to detect small, low-mass planets (of a few Earth radii and masses) because the radial-velocity (RV) signal of low-mass planets and the transit depth of small planets orbiting this type of star are larger than for solar-like stars.

The first piece of evidence that the planet population around M dwarfs is different from that of hotter stars is provided by Endl et al. (2006), who shows that hot Jupiters ($P < 10$ d and $M \sin i > 100 M_{\oplus}$) are rare around M dwarfs compared to solar-like stars. This realization withstands the test of time. Despite favorable sensitivity to hot Jupiters, M dwarf planet surveys result in very few such discoveries (Johnson et al. 2012; Hartman et al. 2015; Bayliss et al. 2018; Bakos et al. 2020). On the other hand, the sample size of the M dwarf surveys that are conducted thus far is not large enough to individually rule out a hot Jupiter occurrence rate that is consistent with that of hot Jupiters around G dwarfs (e.g., Obermeier et al. 2016).

Although the first planets orbiting M dwarfs are discovered by RV surveys (Marcy et al. 2001; Butler et al. 2004; Bonfils et al. 2005), a big leap forward is the *Kepler* satellite (Borucki et al. 2010), which discovers thousands of transiting planets and candidates and shows that the frequency of small planets around low-mass stars, at least in short periods on the order of 100 d, is higher than that around solar-like stars (Howard et al. 2012). Subsequent studies of the *Kepler* sample look at either planet occurrence rates specifically for the M dwarf sample (such as Dressing & Charbonneau 2013, 2015; Hsu et al. 2020) or the stellar mass dependence throughout the full *Kepler* sample (such as Mulders et al. 2015a; Yang et al. 2020). The survey has a very strong focus on G-type stars. Therefore, the size of the M dwarf sample is much lower than that of the G dwarf sample, and the lowest-mass M dwarfs are underrepresented. As an example, only 1.5% (58 stars) of the M dwarfs investigated by Dressing & Charbonneau (2013) have a mass below $0.15 M_{\odot}$. Any study of a mass dependence of planet occurrence rates from the *Kepler* M dwarf sample thus comes with large error bars (Hardegree-Ullman et al. 2019).

An advantage of RV surveys is that they can detect all planets, transiting or not, that induce a sufficiently large velocity variation in their host star. The RV amplitude of a super-Earth planet ($M \sim 3\text{--}5 M_{\oplus}$) in the habitable zone of an M dwarf is on the order of 3 to 5 m s^{-1} , which opens up the thrilling possibility of detecting terrestrial planets orbiting the nearest stars. Nevertheless, the analysis of the M dwarf sample of HARPS (High Accuracy Radial velocity Planet Searcher) by Bonfils et al. (2013) is still the only large statistical analysis of an RV survey of planets around this type of star.

M dwarfs emit most of their light at near-infrared wavelengths. Therefore, red-sensitive optical and infrared spectrographs are better suited for exoplanet surveys than spectrographs working at bluer wavelengths. At these spectral types, the sweet spot with the highest RV precision is the red part of the optical regime and the near infrared, from 700 nm to 900 nm (Reiners et al. 2018b). This consideration leads to the construction of CARMENES (Calar Alto high-Resolution search for M dwarfs with Exo-earths with Near-infrared and optical Echelle Spectrographs; Quirrenbach et al. 2014). CARMENES is a stabilized, fiber-fed, two-channel echelle spectrograph with resolution $R \sim 80\,000\text{--}95\,000$ that covers, in one shot, the wavelength region between 520 nm and 1710 nm. The instrument is operational for over five years and, through its systematic monitoring program, discovers a large number of planets around nearby M dwarfs (see below). As a result, the CARMENES survey is well suited to determine the frequency of planets around low-mass stars. The

CARMENES survey is currently unique because of the large amount of invested observing time and due to it being the first survey to use such a large wavelength range. The CARMENES consortium is awarded 750 useful nights as guaranteed time observations (GTO), which are conducted between January 2016 and December 2020. After its recent completion, the consortium starts a new legacy RV exoplanet survey with a comparable amount of awarded time, which is essentially a continuation of the GTO program. In contrast to previous surveys that use spectrographs in the optical regime like ELODIE, CORALIE, HARPS and the High Resolution Echelle Spectrometer HIRES, the sensitivity of CARMENES to longer wavelengths allows it to focus on M3.0 V to M5.0 V stars, namely, stars that typically have half the mass of the targets studied previously.

Statistics of low-mass planets (with $M_{\text{pl}} < 10 M_{\oplus}$) are not only important for determining their actual frequency, but also for testing theories of planet formation. Most of the existing theories aim to reproduce the planet population in the Solar System and around other solar-like stars and, thus, assume a single solar analog host star (e.g., Ida & Lin 2010; Mordasini et al. 2012b; Ndugu et al. 2018; Emsenhuber et al. 2021; Schlecker et al. 2021a,b). Crucial new insights will emerge from the adaptation of the same underlying theoretical frameworks to planets around low-mass stars and the comparison to observational data.

In this paper, we present planet occurrence rates determined from the first 71 stars for which we have more than 50 observations. After this introduction, we continue in Sect. 2.1 with a short description of CARMENES data in general and of the stellar sample considered in this study. In Sect. 2.2, we describe how we obtained the planet subsample that we use for further analysis. In Sect. 3.1, we describe our injection-and-retrieval experiment to obtain detection limits. We present the method and results of our occurrence rate analysis in Sect. 3.2. The results are discussed in Sect. 4, followed by the conclusions in Sect. 5.

2. Data

Our occurrence rate study is based on 6512 spectra of 71 stars obtained with CARMENES from January 2016 until March 2020. The instrument is located at the 3.5 m telescope of the Calar Alto Observatory in Almería, Spain. The spectra went through the standard GTO data flow and were reduced with the caracal pipeline (Caballero et al. 2016b). We obtained RV information with the SpEctrum Radial Velocity AnaLyser (*serval*) with a precision on the 1 m s^{-1} level (Zechmeister et al. 2018). This precision was reached after we corrected for the nightly zero point, which was derived from a subsample of stars with small RV variability (Trifonov et al. 2018). We base our analysis on the visual channel observations, which cover the wavelength range 520–960 nm, as the RV precision of the visual channel is more suitable for planet detections (but there are detections that combine data from both channels, such as Bauer et al. 2020).

2.1. Stellar sample

The 329 GTO stars of the CARMENES survey are the brightest M dwarfs for their spectral subtype in the input catalog CARMEN(ES) Cool dwarf Information and daTa Archive (Carmencita; Caballero et al. 2016a). From this sample, we excluded stars that turned out to be a spectroscopic binaries. This is usually apparent after a few observations (Baroch et al. 2018).

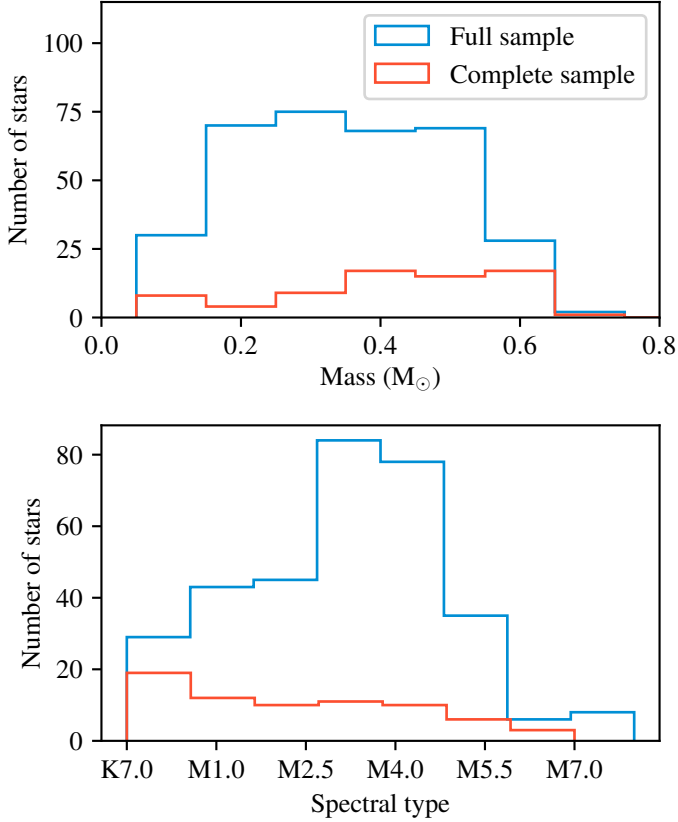


Fig. 1. Histograms of stellar mass (*top panel*) and spectral type (*bottom panel*) of the full GTO CARMENES sample with 329 stars (blue) and the complete subsample with 71 stars (red).

Moreover, we excluded all those stars that were added to the GTO program later, such as the Transiting Exoplanet Survey Satellite (TESS) objects of interest (e.g., [Bluhm et al. 2020](#); [Dreizler et al. 2020](#); [Kemmer et al. 2020](#)), as including them would bias our occurrence rate study. We also excluded very active targets with an RV scatter of more than 10 m s^{-1} and $v \sin i > 2 \text{ km s}^{-1}$, namely “RV-loud” targets (see [Tal-Or et al. 2018](#)). From the remaining sample, we selected the first 71 stars with at least 50 observations, as we do not intend to observe them further.

Figure 1 shows histograms of the stellar mass (M_{\star}) and spectral type of the full sample (329 stars) and the complete subsample (71 stars). The masses of 315 stars in the top panel are taken from [Schweitzer et al. \(2019\)](#). The masses of six stars that are not in the complete sample are calculated with the mass-luminosity-metallicity relation from [Mann et al. \(2019\)](#). In addition, eight stellar masses are dynamical masses from binary stars, which are excluded from our 71 star sample ([Baroch et al. 2018](#)). The median mass of the whole CARMENES sample is $0.348 M_{\odot}$ and that of our subsample is $0.426 M_{\odot}$. Thus, stars more massive than $0.348 M_{\odot}$ are over-represented in our subsample. This is mainly because we excluded the very active RV-loud stars that also have a high RV scatter. Those are more often of lower mass ([Tal-Or et al. 2018](#)).

A histogram of spectral types is shown in the bottom panel of Fig. 1. The spectral type distribution in our complete sample is relatively homogeneous from M0.0 V to M6.0 V (with one K7.0 V target), whereas the full CARMENES GTO sample concentrates more on the spectral types from M3.0 V to M5.0 V.

2.2. CARMENES planets

Several of the published CARMENES planets are discovered in combination with data from other instruments such as HARPS at the European Southern Observatory (ESO) 3.6 m Telescope or HIRES at the Keck I Telescope (e.g., Barnard’s Star b; [Ribas et al. 2018](#)). Since the detection limits are calculated only for the CARMENES survey, our occurrence rate analysis should be based on a planet sample detectable purely from CARMENES data.

The experience from the *Kepler* survey shows that the criteria that are applied for the detection limit method need to be the same to those applied to detect planets ([Gaudi 2021](#)). Furthermore, for the computation of an unbiased occurrence rate, no data from other surveys should be used (cf. [Gaudi 2021](#)). If we include planets from other surveys we do not have the information on the detection limits and survey completeness and we cannot correct for missing planets. We would over-correct the occurrence rates because the planets are below the detection limit of our survey alone (see also Sect. 4). Therefore, we need to identify those planets that we can include in our analysis independently.

We computed generalized Lomb-Scargle (GLS) periodograms ([Zechmeister & Kürster 2009](#)) of all 71 time series. All peaks with a false alarm probability (FAP) of less than 1% were modeled with Keplerian orbits. The models were calculated with the python package PyAstronomy ([Czesla et al. 2019](#)). We subtracted the orbits and looked for periodogram peaks again. If there was a second peak, we modeled both planet candidates with a double Keplerian. We repeated this procedure for up to three signals. Usually, one would repeat the pre-whitening process until no signals with $\text{FAP} < 1\%$ remain in the data. In our data set, though, there are several signals that cannot be removed with a Keplerian model. In addition, a uniform analysis of the signals becomes more challenging when more signals per star are included.

M dwarfs may be active and, therefore, excluding activity peaks is crucial to avoid identifying spurious planet candidates. The activity-induced RV-jitter for a certain activity level is known to be larger in M- than in G-type stars (e.g., [Barnes et al. 2011](#); [Jeffers et al. 2014](#); [Suárez Mascareño et al. 2017](#)). We used four activity indicators to flag the periodogram peaks in this analysis: the $H\alpha$ index and the Ca II infrared triplet (CaIRT), which are sensitive to chromospheric activity, the chromatic index (CRX), which traces the dependence of the RV amplitude on the wavelength, and the differential line width (dLW), which traces changes in the line widths and is an alternative, differential indicator to full width at half maximum. The definition of the four indices is given in [Zechmeister et al. \(2018\)](#) and [Schöfer et al. \(2019\)](#). All indicators were computed by `serval`.

We retrieved 118 periodic signals with $\text{FAP} < 1\%$. We flagged them as either “Planet”, if they corresponded to a published planet, or as “Unsolved”, to be checked further if all of the following criteria apply (see also Table A.1): (i) The period of the signal is shorter than half of our observational time baseline. Otherwise, we could not confirm the periodic nature of this signal. Longer-period signals were flagged as “ $P > \text{time baseline}/2$.” (ii) The signal is not present in any of the four CARMENES activity indicators. If we saw it in any of the activity indicators, we flagged it as “Activity.” (iii) The signal (or its first harmonic) is not near the rotational period tabulated by Carmencita; otherwise, it was flagged as “Rotation.” If a signal that met the period criterion had a very small FAP, $< 10^{-8}$, we skipped the activity analysis and flagged the signal as Unsolved

Table 1. Planets used for occurrence rate calculation.

Karmn		P (d)	$M_{\text{pl}} \sin i$ (M_{\oplus})	RV FAP (%)	Ref.
J01125–169	c	3.060	$1.14^{+0.11}_{-0.10}$	0.0047	Sto20a
J01125–169	d	4.656	$1.09^{+0.12}_{-0.12}$	0.0349	Sto20a
J02530+168	b	4.910	$1.05^{+0.13}_{-0.12}$	$<10^{-6}$	Zec19
J02530+168	c	11.41	$1.11^{+0.16}_{-0.15}$	$<10^{-6}$	Zec19
J03133+047	b	2.291	$3.95^{+0.42}_{-0.43}$	$<10^{-6}$	Bau20
J06548+332	b	14.24	$4.00^{+0.40}_{-0.40}$	$<10^{-6}$	Sto20b
J08413+594	b	203.6	$147^{+7.0}_{-7.0}$	$<10^{-6}$	Mor19
J09144+526	b	24.45	$10.3^{+1.5}_{-1.4}$	0.0012	Gon20
J11033+359	b	12.95	$2.69^{+0.25}_{-0.25}$	$<10^{-6}$	Sto20b
J11417+427	b	41.38	$96.7^{+1.4}_{-1.0}$	$<10^{-6}$	Tri18
J11417+427	c	532.5	$68.1^{+4.9}_{-2.2}$	$<10^{-6}$	Tri18
J11421+267	b	2.644	$21.4^{+0.20}_{-0.21}$	$<10^{-6}$	Tri18
J12123+544S	b	13.67	$6.89^{+0.92}_{-0.95}$	$<10^{-6}$	Sto20b
J12479+097 ^(a)	b	1.467	$2.82^{+0.11}_{-0.12}$	0.0012	Tri21
J13229+244	b	3.023	$8.0^{+0.5}_{-0.5}$	$<10^{-6}$	Luq18
J16167+672S	b	86.54	$24.7^{+1.8}_{-2.4}$	$<10^{-6}$	Rei18
J16303–126 ^(b)	b	1.26	$1.92^{+0.37}_{-0.37}$	0.453	Wri16
J16303–126	c	17.87	$4.15^{+0.37}_{-0.37}$	0.0011	Wri16
J17378+185	b	15.53	$6.24^{+0.58}_{-0.59}$	0.0007	Lal19
J19169+051N	b	105.9	$12.2^{+1.0}_{-1.4}$	$<10^{-6}$	Kam18
J21164+025	b	14.44	$13.3^{+1.0}_{-1.1}$	$<10^{-6}$	Lal19
J21466+668	b	2.305	$2.50^{+0.29}_{-0.30}$	$<10^{-6}$	Ama21
J21466+668	c	8.052	$3.75^{+0.48}_{-0.47}$	$<10^{-6}$	Ama21
J22137–176	b	3.651	$7.4^{+0.5}_{-0.5}$	$<10^{-6}$	Luq18
J2252+594	b	13.35	$16.6^{+0.94}_{-0.95}$	$<10^{-6}$	Nag19
J22532–142	b	61.08	$242^{+0.7}_{-0.7}$	$<10^{-6}$	Tri18
J22532–142	c	30.13	$761^{+1.0}_{-1.0}$	$<10^{-6}$	Tri18

Notes. ^(a)We tabulate the actual mass of the transiting planet GJ 486 (J12479+097). ^(b)The orbital period of GJ 628 b (J16303–126) reported by Wri16 was 4.89 d.

References. Ama21: Amado et al. (2021); Bau20: Bauer et al. (2020); Gon20: González-Álvarez et al. (2020); Kam18: Kaminski et al. (2018); Lal19: Lalitha et al. (2019); Luq18: Luque et al. (2018); Mor19: Morales et al. (2019); Nag19: Nagel et al. (2019); Rei18: Reiners et al. (2018a); Sto20a: Stock et al. (2020a); Sto20b: Stock et al. (2020b); Tri18: Trifonov et al. (2018); Tri21: Trifonov et al. (2021); Wri16: Wright et al. (2016); Zec19: Zechmeister et al. (2019).

or Planet in any case because such a signal needed to be analyzed manually.

The automated signal detection process returned 27 planets (with published data) and another 18 signals flagged as Unsolved. The Unsolved signals are most probably caused by stellar activity. We reach this conclusion because their amplitude and phase are not stable over time or because the signal is a second harmonic of the rotation period.

The 27 planets that were identified in this way are only those planets for which the CARMENES observations were already thoroughly investigated and published. All these planets and the

corresponding CARMENES publications are listed in Table 1. The only exception is a planetary system discovered by Wright et al. (2016) with HARPS around GJ 628 (J16303–126). We identify the signals of the two inner planets in our periodograms. However, we find the inner planet GJ 628 b at 1.26 d – an alias of the published period at 4.89 d. We also obtain a higher RV amplitude of $2.42^{+0.39}_{-0.32}$ m s⁻¹ as compared to $1.67^{+0.20}_{-0.19}$ m s⁻¹ in a newer publication on this planet (Astudillo-Defru et al. 2017). This amplitude discrepancy and ambiguity in period need more thorough investigation. We include this planet with the parameters derived from our data (see Table A.1). The new period and $M_{\text{pl}} \sin i$ are close enough to the ones that are published such that this will not affect our occurrence rate conclusions.

3. Analysis and results

3.1. Planet detection completeness

The completeness of the planet detections in our sample was calculated with an injection-and-retrieval experiment similar to other occurrence rate studies (e.g., Cumming et al. 1999; Zechmeister & Kürster 2009; Meunier et al. 2012; Bonfils et al. 2013). In particular, we injected single planets with circular orbits into our RV data and tested if we could retrieve them with a GLS periodogram (the effect of eccentric orbits is discussed in Sect. 4.2). For this purpose, we created a log-uniform grid in planet minimum mass, $M_{\text{pl}} \sin i$, and period, P , of 60 grid points each in the ranges 1–10 000 M_{\oplus} and 1–10 000 d, respectively, and used those mass-period combinations as parameters for our injected test planets. For circular orbits the amplitude of the simulated RV curves was computed by the approximation:

$$K = 28.435 \text{ m s}^{-1} \left(\frac{P}{1 \text{ yr}} \right)^{-1/3} \left(\frac{M_{\text{pl}} \sin i}{M_{\text{Jup}}} \right) \left(\frac{M_{\star}}{M_{\odot}} \right)^{-2/3}. \quad (1)$$

There are two possible approaches on how to include measurement errors: we could calculate the standard deviation of the pre-whitened data set and add random noise with the same standard deviation (cf. Cumming et al. 1999) or inject the planet signal directly into the pre-whitened observed RV data (see, e.g., Bonfils et al. 2013). We used the second method since it avoids any assumption on the distribution of measurement uncertainties. Another advantage is that this approach preserves the stellar activity signal. The RVs of the simulated time series are then:

$$RV(t) = K \sin \left(\frac{2\pi t}{P} + \phi \right) + RV_{\text{observed}}(t), \quad (2)$$

where P is the period of the planetary orbit, ϕ is a random phase angle, $RV_{\text{observed}}(t)$ is the RV at the time stamp after pre-whitening, and t is the time stamp of the observation. The RV semi-amplitude K is derived from the projected mass $M_{\text{pl}} \sin i$ assigned to the planet (Eq. (1)).

We obtained a detection map as a function of $M_{\text{pl}} \sin i$ and P for every star in our sample as follows. We simulated the RV signals of 50 test planets at each grid point ($M_{\text{pl}} \sin i, P$) with randomized phase angles, according to the prescriptions outlined above. Then, we injected each signal into the star's pre-whitened RV data and attempted to recover them. The criteria for a successful recovery were that the highest peak of the GLS periodogram has a FAP < 1% and is at the same period as the injected period (the tolerance is the peak width, which is the inverse of the time span in frequency space). The detection probability at every grid point is then the ratio of retrieved to

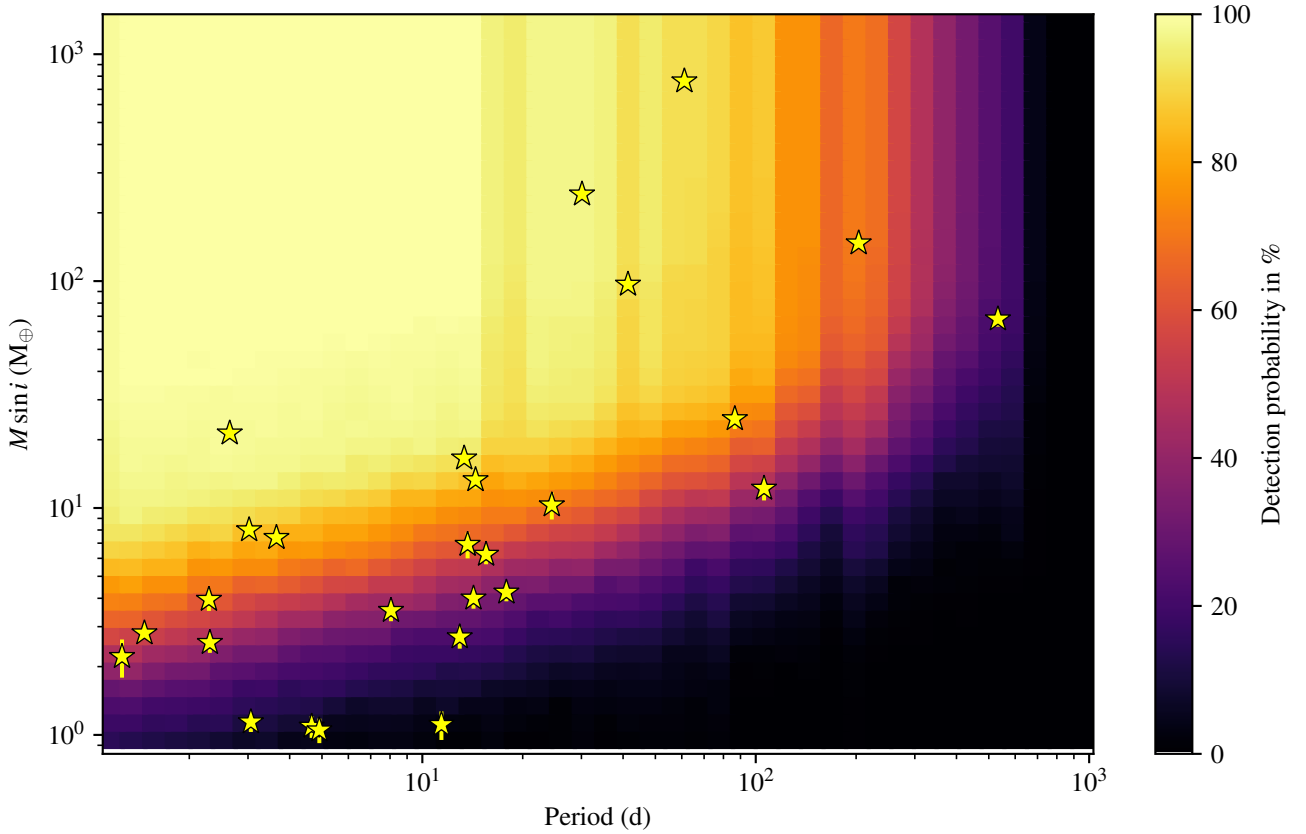


Fig. 2. CARMENES GTO survey detection completeness for the subsample of 71 stars. The color map indicates the average detection probability of the corresponding period-mass combination. Yellow stars indicate planets discovered by CARMENES (error bars are sometimes smaller than the marker size).

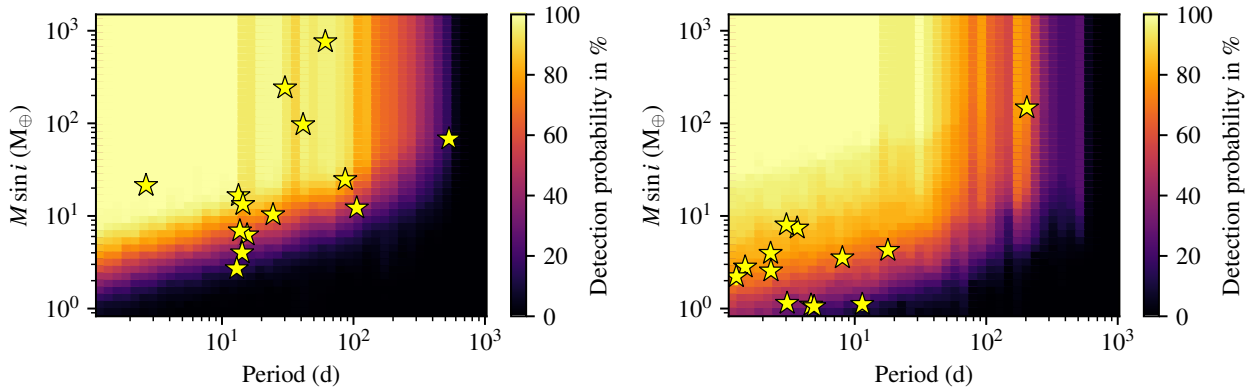


Fig. 3. Same as Fig. 2 but for the subsamples of 48 stars with $M_* > 0.34 M_\odot$ (left) and of 23 stars with $M_* < 0.34 M_\odot$ (right).

injected planets: $p_{\text{pl, det},i}(M_{\text{pl}} \sin i_i, P_i) = N_{\text{retrieved},i}/N_{\text{injected},i}$. The detection map of the whole survey, shown in Fig. 2 (and Fig. 3 for two stellar mass bins), is then an average detection probability of every $M_{\text{pl}} \sin i$ and period combination.

Figure 4 presents the survey sensitivity in a different way. It shows that we cannot detect Earth-mass planets around stars more massive than $0.34 M_\odot$. The detection probability increases steeply for planets of $2 M_\oplus$ or more. Around later (i.e., less massive) M dwarfs, our CARMENES RV survey is able to detect some Earth-mass planets. We chose $M \sin i = 0.34 M_\odot$ as the dividing line between early- and late-type M dwarfs. This mass boundary corresponds approximately to spectral type M3.5 V and $T_{\text{eff}} \approx 3300$ K and the threshold between fully and not fully convective stars (Cifuentes et al. 2020).

3.2. Occurrence rates

To finally obtain the occurrence rates, we ran a Monte Carlo simulation. For this purpose, we created a grid of test planet frequencies \bar{n}_{pl} in number of planets per star. For each of those test frequencies, we wanted to obtain the probability that this frequency is consistent with the number of planets $N_{\text{pl,det}}$ that were detected in this period-mass bin.

Therefore, each simulation run followed the following four steps: (i) We drew a number of test planets, $N_{\text{pl,in}}$, that corresponds to the test planet frequency from a Poisson distribution with $\lambda = \bar{n}_{\text{pl}} N_*$ (where N_* is the number of stars in the sample). (ii) We assigned every test planet a minimum mass, $M_{\text{pl}} \sin i$, and orbital period, P , from the mass-period grid of our detection

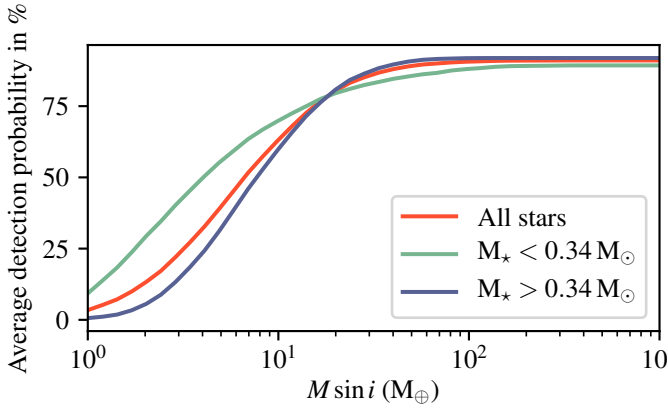


Fig. 4. Average planet detection probabilities of the complete sample (subsample of 71 CARMENES GTO stars) as a function of projected planet mass averaged over the period range 1–240 d. The three curves depict the probabilities for early-M (blue), late-M (green), and all stars (red). The maximum probability is 0.91 on average.

map. (iii) We accepted the test planet as a planet detection with the detection probability at the given $M_{\text{pl}} \sin i$ and P . (iv) We counted the number of test planet retrievals, $N_{\text{pl,out}}$.

We ran this simulation 200 times for every test frequency and counted the number of times that $N_{\text{pl,out}}$ was equal to $N_{\text{pl,det}}$. The resulting probability density was normalized such that the sum of all points was 1. We show a binned version of the simulation output in Fig. 5. We utilized the cumulative probability at the 16%, 50%, and 84% levels as the lower limit, median and upper limits, respectively. Where we derived upper limits (for bins where $N_{\text{pl,det}} = 0$), we took the 84% level as an upper limit. This method is a variant of the method used by Bonfils et al. (2013) with the HARPS M dwarf sample.

Bonfils et al. (2013) repeatedly drew N_* random probabilities in every bin and took the 16% and 84% levels of the resulting distribution as error bars. If the probabilities are randomly drawn from the $\log P$ - $\log M_{\text{pl}} \sin i$ grid, it is implicitly assumed that the planet $M_{\text{pl}} \sin i$ and P are log-uniformly distributed. However, we know from *Kepler* that this is probably true neither for the period (Mulders et al. 2015a) nor for the radius (e.g., Foreman-Mackey et al. 2014) distributions of small planets. Nevertheless, we adapted the assumption of a log-uniform distribution in period and discuss why this assumption does not bias our results significantly in Sect. 4. For the mass, on the other hand, we used two power-law distributions, whose parameters we infer below.

In Fig. 6, we show a histogram of the CARMENES planet detections. Every minimum mass bin of this histogram was corrected with a correction factor C , which is the inverse of the average detection efficiency per bin (see Fig. 4). As a result, we obtained corrected numbers of planets $N_{\text{pl,corr}} = C N_{\text{pl,det}}$ for six bins of $M_{\text{pl}} \sin i$. We fit those six data points with two power laws of the type:

$$N_{\text{pl}} = a(M_{\text{pl}} \sin i)^\alpha, \quad (3)$$

with the breaking point at $32 M_\oplus$ ($0.1 M_{\text{Jup}}$). We measured $\alpha = -0.26 \pm 0.17$ for planets with $M_{\text{pl}} \sin i > 32 M_\oplus$ and $\alpha = -1.14 \pm 0.16$ for planets with $M_{\text{pl}} \sin i < 32 M_\oplus$.

The minimum mass we gave every test planet in step 2 from above is drawn from this mass distribution. The resulting occurrence rates are shown in Fig. 7.

Table 2. Planet occurrence rates (part 1).

(a) All M stars of the sample (71 stars)		
P (d)		
1–10	10–100	100–1000
$N_{\text{pl,det}} = 0$	$N_{\text{pl,det}} = 2$	$N_{\text{pl,det}} = 1$
$\bar{n}_{\text{pl}} < 0.03$	$\bar{n}_{\text{pl}} = 0.04^{+0.03}_{-0.02}$	$\bar{n}_{\text{pl}} = 0.05^{+0.04}_{-0.03}$
(b) M stars with $M_* > 0.34 M_\odot$ (48 stars)		
P (d)		
1–10	10–100	100–1000
$N_{\text{pl,det}} = 0$	$N_{\text{pl,det}} = 2$	$N_{\text{pl,det}} = 0$
$\bar{n}_{\text{pl}} < 0.04$	$\bar{n}_{\text{pl}} = 0.06^{+0.04}_{-0.03}$	$\bar{n}_{\text{pl}} < 0.07$
(c) M stars with $M_* < 0.34 M_\odot$ (23 stars)		
P (d)		
1–10	10–100	100–1000
$N_{\text{pl,det}} = 0$	$N_{\text{pl,det}} = 0$	$N_{\text{pl,det}} = 1$
$\bar{n}_{\text{pl}} < 0.08$	$\bar{n}_{\text{pl}} < 0.08$	$\bar{n}_{\text{pl}} = 0.16^{+0.15}_{-0.09}$

Notes. Planet occurrence rates of CARMENES planets in the minimum mass range of $100 M_\oplus$ to $1000 M_\oplus$. \bar{n}_{pl} : average number of planets per star; $N_{\text{pl,det}}$: number of detected planets.

3.3. Planets with $M_{\text{pl}} \sin i$ between $100 M_\oplus$ and $1000 M_\oplus$

In Table 2 and the upper panel of Fig. 7, we show the resulting occurrence rates for giant planets with $M_{\text{pl}} \sin i > 100 M_\oplus$. As we do not detect any hot Jupiter ($P < 10$ d) in our sample, we place an upper bound on their occurrence rate at 0.03 planets per star. The most massive close-in planet that we find with CARMENES is GJ 436 b (originally discovered by Butler et al. 2004 and reanalyzed by Trifonov et al. 2018), with a mass of $21.4 M_\oplus$. The paucity of hot Jupiters is also observed in all previous RV surveys of M dwarfs (Endl et al. 2006; Zechmeister et al. 2009; Bonfils et al. 2013). The Exoplanet Encyclopædia lists only four confirmed hot Jupiters around M dwarfs, all at very long heliocentric distances ($d > 140$ pc): Kepler-45 b (Johnson et al. 2012), HATS-6 b (Hartman et al. 2015), NGTS-1 b (Bayliss et al. 2018), and HATS-71 A b (Bakos et al. 2020).

In comparison, the hot Jupiter occurrence rate from G-dwarf RV surveys is 1.1–1.6% (Wright et al. 2012; Howard et al. 2010). As our upper limit does not exclude this hot Jupiter frequency, a larger sample size is needed to confirm the lower occurrence rate of hot Jupiters around M dwarfs than around G dwarfs. At orbits from 10 d to 1000 d, the giant planet fraction increases to $0.06^{+0.04}_{-0.03}$ planets per star. The M dwarf giant planets reside in longer orbits and their overall fraction is comparable to that of gas giants around G dwarfs ($5.2\% \pm 0.6\%$ in Cumming et al. 2008). However, this statement has to be taken with caution as the high frequency of gas giants in our sample is affected by a selection bias (see further details in Sect. 4). The frequency of M dwarf gas giants in the full sample with about five times as many targets could be up to a factor of five lower.

To explore the planet population dependence on host star mass, we split the sample into two groups of host star mass. We set the threshold between the groups at $M_* = 0.34 M_\odot$ (see Sect. 3.1). In the group of more massive, early M dwarfs there are 48 stars and in the group of less massive, late M dwarfs there are 23 stars. Within each subgroup, we repeated the occurrence rate calculations as described above. The resulting occurrence rates of both groups are also shown in Table 2. Due to the lower

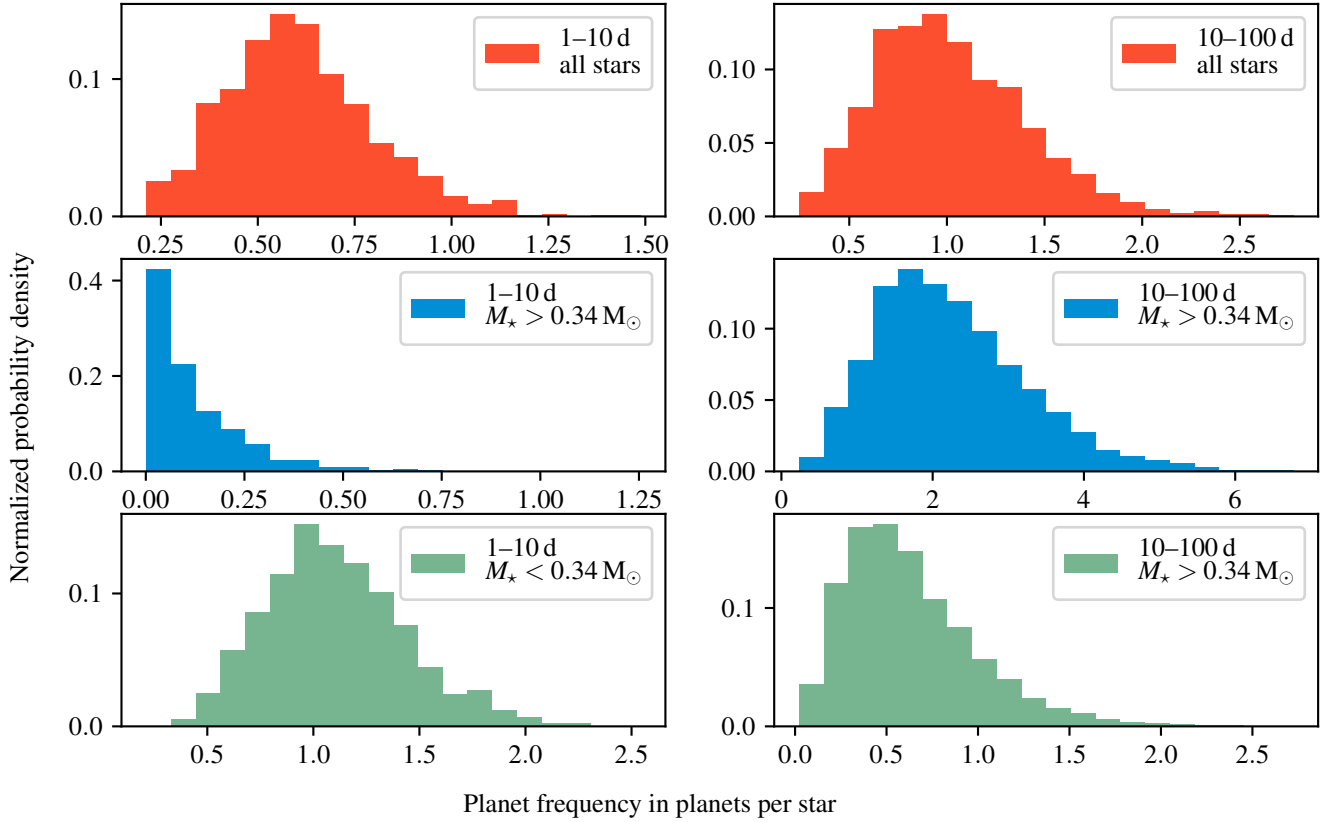


Fig. 5. Output of the Monte Carlo simulation for planets with $1 M_{\oplus} < M_{pl} < 10 M_{\oplus}$. The probability density is normalized such that the sum of all discrete points is unity.

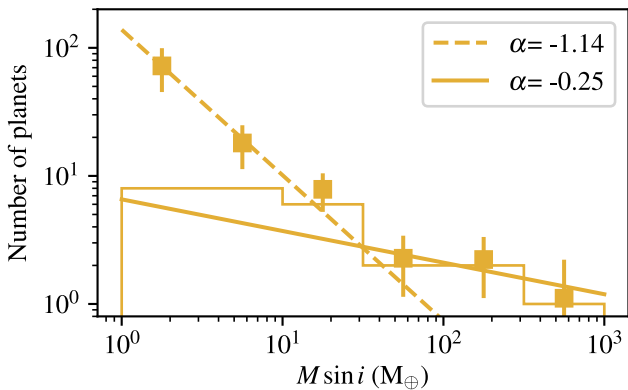


Fig. 6. Number of CARMENES planet detections as a function of planet mass. The histogram shows the number of CARMENES planet detections and the squares the number of planets corrected for survey sensitivity. The dashed line is a power law fit to the corrected number of planets in the bins with $M_{pl} < 32 M_{\oplus}$, and the solid line is a power law fit to the bins with $M_{pl} > 32 M_{\oplus}$.

number of stars in each group, the uncertainties of those results are higher. We show detection maps of the stellar mass subsamples in Fig. 3. In the region of periods longer than 100 d, our detection efficiency becomes low even for the high-mass planets. This is due to the strict period cutoff at half the time baseline of the observations. The median time baseline of the observations of our sample is 1124 d.

We detect only one giant planet around our less massive stars, which is the exceptional case of GJ 3512 b (Morales et al. 2019).

This $\sim 150 M_{\oplus}$ mass planet orbits a very low-mass star of only $0.12 M_{\odot}$. In addition, we confirm two giant planets around a host that is in our group of more massive stars: GJ 876 b,c (Trifonov et al. 2018).

3.4. Planets with $M_{pl} \sin i$ between $10 M_{\oplus}$ and $100 M_{\oplus}$

In Table 3 and the middle panel of Fig. 7, we show the resulting occurrence rates for planets with minimum masses from $10 M_{\oplus}$ – $100 M_{\oplus}$. The occurrence rate of those intermediate-mass planets, including Saturns, Neptunes, and, perhaps, large super-Earths, increases from short-period orbits to long-period orbits. Again, we split the sample in the same stellar mass bins as described in the previous section. We find eight planets in this mass-period regime around the more massive stars, while we find no planets around our less massive stars. An analysis of the occurrence rates shows that from our upper limits we cannot tell if the population of intermediate-mass planets around our more massive stars is different from that of our less massive stars.

3.5. Planets with $M_{pl} \sin i$ between $1 M_{\oplus}$ and $10 M_{\oplus}$

The occurrence rates of our low-mass planets are shown in Table 4 and the lower panel of Fig. 7. As expected, the low-mass planets ($M < 10 M_{\oplus}$, i.e., Earths and super-Earths) are the most abundant type of planets in our sample. We detect ten planets close to their host star at periods less than 10 d and six planets at intermediate periods of 10–100 d. The occurrence rates are also high with about 0.59 and 0.97 planets per star, respectively. There is a slight indication that the planet frequency increases toward long periods, but our results are also consistent with a

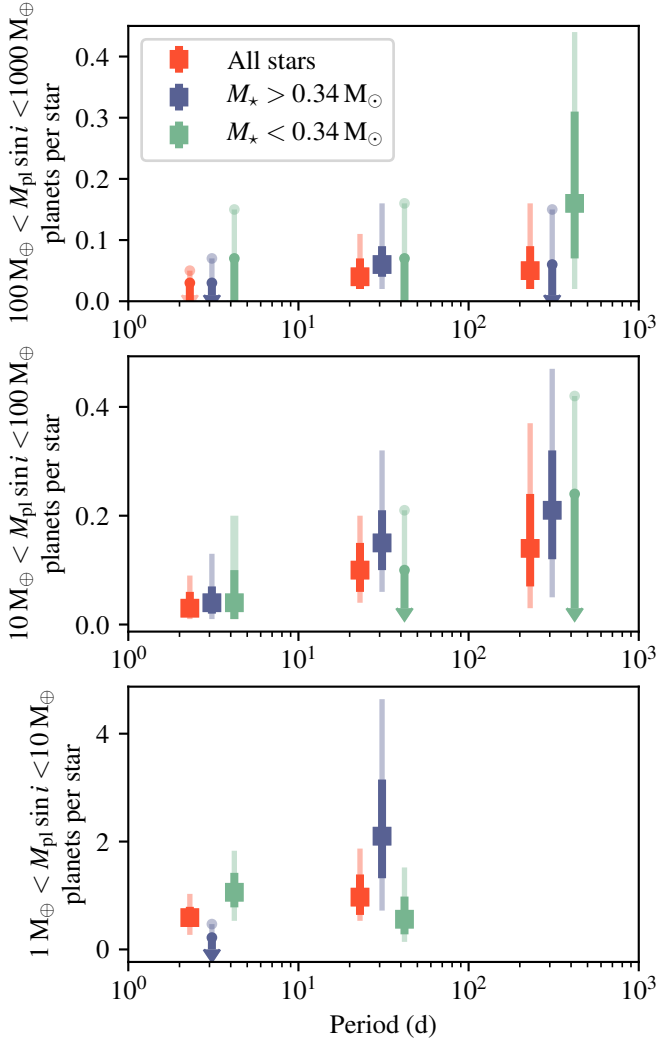


Fig. 7. CARMENES M dwarf exoplanet occurrence rates as a function of orbital period for three different planetary mass intervals. Error bars are the 16% and 84% of the output distribution, and transparent error bars are the 2.5% and 97.5% of the output distributions. The occurrence rates of the upper panel might suffer from a selection bias (see Sect. 4). The colors have the same meaning as in Fig. 4.

flat occurrence rate distribution. From the results of transit surveys, we expect an overall higher number of low-mass planets around M dwarfs than around G dwarfs (e.g., Howard et al. 2012; Mulders et al. 2015a; Yang et al. 2020). Mayor et al. (2011) derived a frequency of low-mass planets of 0.41 ± 0.16 planets per star with periods of up to 50 d around G-type stars. In order to compare our results to this planet frequency, we ran our simulation again with the same period constraint. The resulting low-mass planet frequency of our M dwarf sample is $1.18^{+0.31}_{-0.27}$ planets per star. Our results, therefore, confirm a three times higher low-mass planet occurrence rate around M dwarfs.

We again computed the occurrence rates split in the two bins of stellar mass (see Table 4). All the low-mass planets of our sample with hosts with stellar masses of $M_* > 0.34 M_\odot$ reside in orbits longer than 10 d. This means that in our earlier M dwarfs there is an increase in the low-mass planet occurrence rate toward long periods. In the lower mass stellar sample, on the other hand, there is a decreasing planet occurrence or a plateau toward long periods.

Table 3. Planet occurrence rates (part 2).

(a) All M stars of the sample (71 stars)		
P (d)		
1–10	10–100	100–1000
$N_{\text{pl,det}} = 1$	$N_{\text{pl,det}} = 5$	$N_{\text{pl,det}} = 2$
$\bar{n}_{\text{pl}} = 0.03^{+0.03}_{-0.01}$	$\bar{n}_{\text{pl}} = 0.10^{+0.05}_{-0.04}$	$\bar{n}_{\text{pl}} = 0.14^{+0.10}_{-0.07}$
(b) M stars with $M_* > 0.34 M_\odot$ (48 stars)		
P (d)		
1–10	10–100	100–1000
$N_{\text{pl,det}} = 1$	$N_{\text{pl,det}} = 5$	$N_{\text{pl,det}} = 2$
$\bar{n}_{\text{pl}} = 0.04^{+0.04}_{-0.02}$	$\bar{n}_{\text{pl}} = 0.15^{+0.07}_{-0.05}$	$\bar{n}_{\text{pl}} = 0.21^{+0.13}_{-0.10}$
(c) M stars with $M_* < 0.34 M_\odot$ (23 stars)		
P (d)		
1–10	10–100	100–1000
$N_{\text{pl,det}} = 0$	$N_{\text{pl,det}} = 0$	$N_{\text{pl,det}} = 0$
$\bar{n}_{\text{pl}} < 0.10$	$\bar{n}_{\text{pl}} < 0.10$	$\bar{n}_{\text{pl}} < 0.24$

Notes. Planet occurrence rates of CARMENES planets in the minimum mass range of $10 M_\oplus$ to $100 M_\oplus$. \bar{n}_{pl} : average number of planets per star; $N_{\text{pl,det}}$: number of detected planets.

Table 4. Planet occurrence rates (part 3).

(a) All M stars of the sample (71 stars)		
P (d)		
1–10	10–100	100–1000
$N_{\text{pl,det}} = 10$	$N_{\text{pl,det}} = 6$	$N_{\text{pl,det}} = 0$
$\bar{n}_{\text{pl}} = 0.59^{+0.20}_{-0.17}$	$\bar{n}_{\text{pl}} = 0.97^{+0.42}_{-0.33}$...
(b) M stars with $M_* > 0.34 M_\odot$ (48 stars)		
P (d)		
1–10	10–100	100–1000
$N_{\text{pl,det}} = 0$	$N_{\text{pl,det}} = 4$	$N_{\text{pl,det}} = 0$
$\bar{n}_{\text{pl}} < 0.22$	$\bar{n}_{\text{pl}} = 2.10^{+1.13}_{-0.81}$...
(c) M stars with $M_* < 0.34 M_\odot$ (23 stars)		
P (d)		
1–10	10–100	100–1000
$N_{\text{pl,det}} = 10$	$N_{\text{pl,det}} = 2$	$N_{\text{pl,det}} = 0$
$\bar{n}_{\text{pl}} = 1.06^{+0.35}_{-0.28}$	$\bar{n}_{\text{pl}} = 0.55^{+0.40}_{-0.26}$...

Notes. Planet occurrence rates of CARMENES planets in the minimum mass range of $1 M_\oplus$ to $10 M_\oplus$. \bar{n}_{pl} : average number of planets per star; $N_{\text{pl,det}}$: number of detected planets.

4. Discussion

4.1. Assumptions and simplifications

To measure occurrence rates, we make several assumptions and simplifications, elaborated below.

No false positives. All planets included in this study are carefully analyzed. In the respective publications, the authors tested at least three activity indicators, orbit stability, and, in some cases, dynamical stability. All the planet signals have a very low FAP. Therefore, we assume that none of our planet candidates is a false positive.

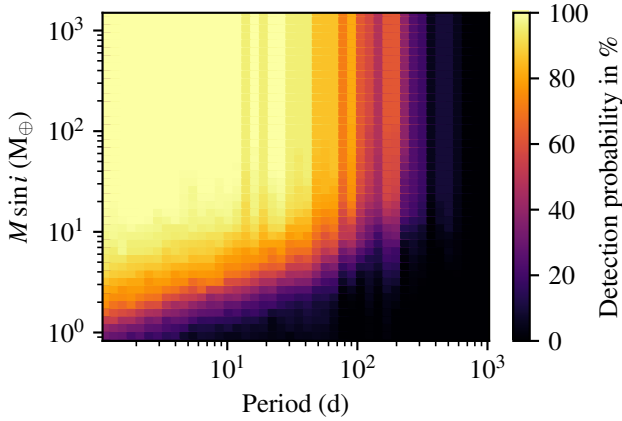


Fig. 8. Same as Fig. 2 but for the subsample of 21 planet host stars.

Unbiased sample. In any occurrence rate study, we need to be aware of the selection biases that could alter the statistics. When the original GTO sample was selected, the only selection criteria were spectral type, J -band magnitude, absence of known companions at less than 5 arcsec, and visibility from the Calar Alto Observatory. After a few spectra were taken, new spectroscopic binaries were identified and excluded from the sample. This is usually done in RV surveys (e.g., with HARPS and CORALIE by Mayor et al. 2011) and is sometimes done in transit survey analysis as well (e.g., in the *Kepler* occurrence rate analysis of rocky habitable zone planets by Bryson et al. 2021). The results are most certainly different if close binary stars are kept in the sample (e.g., Moe & Kratter 2021). Therefore, this bias should be kept in mind if the results are compared to surveys that use other planet detection methods or artificial planet populations from planet formation theory. It should be noted that wide multiplicity does not affect our sample selection nor our RV survey (e.g., Kaminski et al. 2018; Trifonov et al. 2018; González-Álvarez et al. 2020).

In addition to that, our subsample of 71 stars out of the full GTO sample of 329 stars is not predefined. A high-mass planet can be identified with fewer observations than a low-mass planet. For this reason, planet detections of high-mass planets could be over-represented in the 71-star sample. If we do not find any additional giant planets in the rest of the 329 star sample, their occurrence rates will be up to a factor of five lower. An analysis of the full sample will give less biased giant planet occurrence rates.

Furthermore, many RV surveys observe targets with interesting signals more often than the rest of the sample. In this way, the detection limits of planet-hosting stars are at lower $M_{\text{pl}} \sin i$ than the detection limits of those without any planetary signal, as shown in Fig. 8. This could lead to an overestimation of the occurrence rates in the low-mass bins where the difference is the largest. We minimize this bias by already accepting test planets at a FAP as high as 1% and averaging the occurrence rates over large bins of the $M_{\text{pl}} \sin i$ -period plane.

Power-law distribution of injected $M_{\text{pl}} \sin i$. The power law that we determine as the underlying distribution is not very well constrained. Both power law fits are made to only three or four points. Still, this distribution is a much better approximation of the true underlying distribution than a log-uniform one. Choosing a realistic distribution from which to draw planets for the injection-recovery tests is especially important in the bins that contain large heterogeneities or gradients in detection sensitivity.

As a comparison, in the lowest-mass bin with $1 M_{\oplus} < M_{\text{pl}} \sin i < 10 M_{\oplus}$, we calculate planet occurrence rates of $0.35^{+0.12}_{-0.10}$ and $0.47^{+0.20}_{-0.15}$ planets per star for the 1–10 d and the 10–100 d bins, respectively, if we assume a log-uniform distribution of the injected $M_{\text{pl}} \sin i$. This is almost a factor of two lower than the rates that we obtain with a more realistic mass distribution.

Log-uniform distribution of period. Since the detection probability varies only weakly with period (e.g., 0–20% in P and 0–80% in $M_{\text{pl}} \sin i$) within the chosen bins, the assumption of the distribution of P is less critical compared to the one for $M_{\text{pl}} \sin i$. A strong period dependence of the true occurrence rate, for which we see no evidence in our data, would thus not affect our analysis significantly.

Correct choice of method. We test other methods to determine detection limits and to retrieve planet occurrence rates. For the detection limits, we also use the method shown by Howard et al. (2010). They did not perform an injection-and-retrieval experiment but fit sinusoids to the data for a dense grid of orbital periods. The amplitude of the fit was considered as the detection limit. When we calculated the detection limits in this way, we retrieved detection limits that were up to a factor two lower than those calculated in Sect. 3.1. We consider the detection limits described in Sect. 3.1 to be more realistic because the way with which we retrieve them is closer to the way with which we actually identify planet candidates. Nevertheless, the resulting occurrence rates are consistent in the high-mass bins. In the low-mass bins, the occurrences are lower (as expected with lower detection limits), but still consistent within the error bars.

For retrieving planet occurrence rates, we also use the inverse detection efficiency method (IDEM), which is widely used in the literature (e.g., Cumming et al. 2008; Wittenmyer et al. 2020). The computed occurrence rates with this method are consistent in all period-mass bins with those described in Sect. 3.2. The main difference is that instead of an increasing occurrence rate with longer periods, we measure the same occurrence rate of 0.65 ± 0.2 planets per star in both low-mass bins with $M_{\text{pl}} \sin i < 10 M_{\oplus}$. The reason for this is that this result is slightly dominated by four very low-mass planets around very low-mass stars (namely Teegarden’s Star b,c and ; Zechmeister et al. 2019, Stock et al. 2020a). Within IDEM, those planets get a much higher weight than the other planets. The results of this method, therefore, confirm the observational evidence of the low-mass planets of low-mass stars residing in shorter-period orbits than those of stars with higher mass.

Circular orbits. We fix the eccentricity of the Keplerian orbits to zero. The consequence of this choice is explored in detail in Sect. 4.2.

Separability. We make use of the so-called approximation of separability (Tremaine & Dong 2012): We treat multi-planet systems as several single-planet systems. Again, this is explained in detail in Sect. 4.2.

4.2. Multi-planet systems and eccentric orbits

Our occurrence rate analysis is based on injection-and-retrieval experiments involving single-planets in circular orbits. This is of course an idealized setup, since many M dwarf planets reside in multi-planet systems (e.g., TRAPPIST-1; Gillon et al. 2017) and some are on eccentric orbits. Therefore, it is important to assess the impact of realistic planet multiplicity and orbital eccentricity distributions on our conclusions.

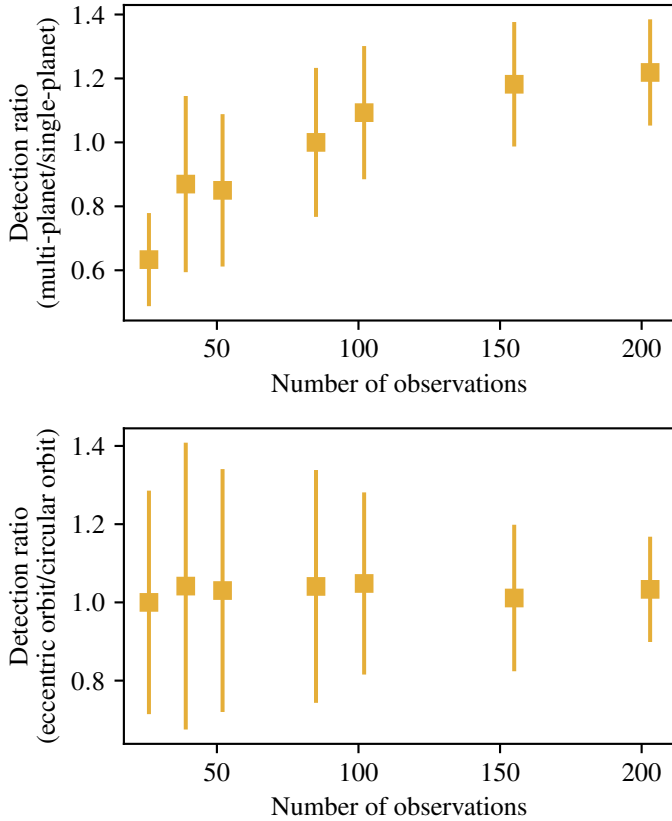


Fig. 9. Ratio of retrieved planets from injection-and-retrieval experiments with test planets in multi-planet test systems (*upper panel*) or on eccentric orbits (*lower panel*), compared to the same experiment with corresponding planets in single-planet systems or on circular orbits, respectively. Error bars are 16% and 84% of the simulation outcomes.

The “approximation of separability” (Tremaine & Dong 2012) states that one can treat a multi-planet system like several single-planet systems with identical host stars. Therefore, we are interested in the ratio of detectable single-planet hosts in comparison to multi-planet hosts. If the approximation of separability is true, the N_{hosts} that we can determine in a sample of multi-planet systems should be the same as that of a sample of identical single-planet systems that consist only of the planet of the first sample with the highest K amplitude. We test this approximation with a set of artificial multi-planet systems. Our test systems are taken from a synthetic population created with the Generation 3 Bern Model (Emsenhuber et al. 2021), which was recently extended to M dwarf hosts (Burn et al. 2021). Almost all of the test systems are multi-planet systems with several planets. We ran an injection-and-retrieval experiment with those test planets. From the whole set of systems, we randomly drew 71 systems and calculated the corresponding RV curves. Our measurement errors and time stamps were taken from actual CARMENES observations of different stars with different numbers of RV values. The first simulation run was done on the whole test planet set. In a second run, we included only the planets with the highest RV semi-amplitude of each planetary system. The resulting ratio of retrieved planet hosts of multi-planet systems versus retrieved planet hosts of single-planet systems is plotted in the upper panel of Fig. 9. In the case of only 26 RV values, we still retrieve about 60% of the multi-planet hosts compared to the single-planet hosts. At the level of 50 observations, the ratio is 80%. This number increases with the number of observations

and, starting from about 80 observations, we retrieve the same number of multi-planet and single-planet hosts.

The sensitivity of periodogram analysis is hardly affected by the orbital eccentricity as long as $e \leq 0.4$ (Cumming 2004). Kipping (2013) published an observed eccentricity distribution from known RV planets. Of those planets, 80% had an eccentricity of 0.4 or less. Nevertheless, we ran a simulation similar to that for the multi-planet systems. We took the single planets on eccentric orbits as the first set of test systems and the same planets on circular orbits as the second set of test systems. The result of the simulation is shown in the lower panel of Fig. 9. The ratio is close to one even for a small number of observations. For these reasons, the simplifications made in the injection-and-retrieval tests are not expected to bias our analysis statistically.

4.3. Comparison to the HARPS M dwarf survey

The largest previous RV study of M dwarfs is the HARPS M dwarf survey (Bonfils et al. 2013). It includes 102 stars and 14 reported planets¹. The extreme precision RV spectrograph HARPS covers the wavelength range 378–691 nm and, therefore, does not observe the range 700–900 nm, which is the sweet spot for M dwarf observations (Reiners et al. 2018a). Nevertheless, the median stellar mass of the HARPS sample is $0.29 M_{\odot}$ and, thus, lower than that of our CARMENES complete sample, which is $0.43 M_{\odot}$ (see upper panel of Fig. 10). The median masses of the planet host stars in both surveys are very similar as well, with $0.35 M_{\odot}$ and $0.33 M_{\odot}$ for the CARMENES complete sample and the HARPS M dwarf sample, respectively. The main difference is that the CARMENES planet host stars have a wider range of masses from $0.09 M_{\odot}$ to $0.70 M_{\odot}$, as compared to a range from $0.31 M_{\odot}$ to $0.49 M_{\odot}$ of the HARPS planet hosts (see also upper panel of Fig. 10). A comparison of the number of observations per spectral type of the two surveys (lower panel of Fig. 10) shows that the CARMENES observations are spread out more homogeneously over the spectral type range whereas the HARPS observations focus more on spectral types M1.0 V–M4.0 V. A direct comparison of the Bonfils et al. (2013) occurrence rates with those of CARMENES is presented in Fig. 11. The results are largely consistent. Only in the 10–100 d and 10–100 M_{\oplus} bin the CARMENES occurrence rate is higher. In this bin, CARMENES detected five planets, whereas Bonfils et al. (2013) reported zero detections. Two of the CARMENES planets are detected around M0.0 V stars for which there are a lot more RV values from CARMENES than from HARPS. The upper limit of the HARPS data is lower than the 2.5% output of our simulations (see Fig. 11). It is possible that intermediate-mass planets are more frequent around earlier M dwarfs, as expected within the core accretion framework (e.g., Burn et al. 2021). In this case, the explanation for this is probably a combination of a better representation of early M dwarfs in the CARMENES measurements and a statistical effect. A statistical analysis with more data from the HARPS M dwarf sample or of the full CARMENES sample should show if this result remains significant.

4.4. Comparison to small planets from Kepler

Other widely used planet occurrence rates of M dwarfs are those derived from results of the *Kepler* space mission. The various

¹ The HARPS planet sample includes the former planet candidate GJ 581 d, which is most probably an activity signal and, therefore, a false positive (Robertson et al. 2014; Hatzes 2016).

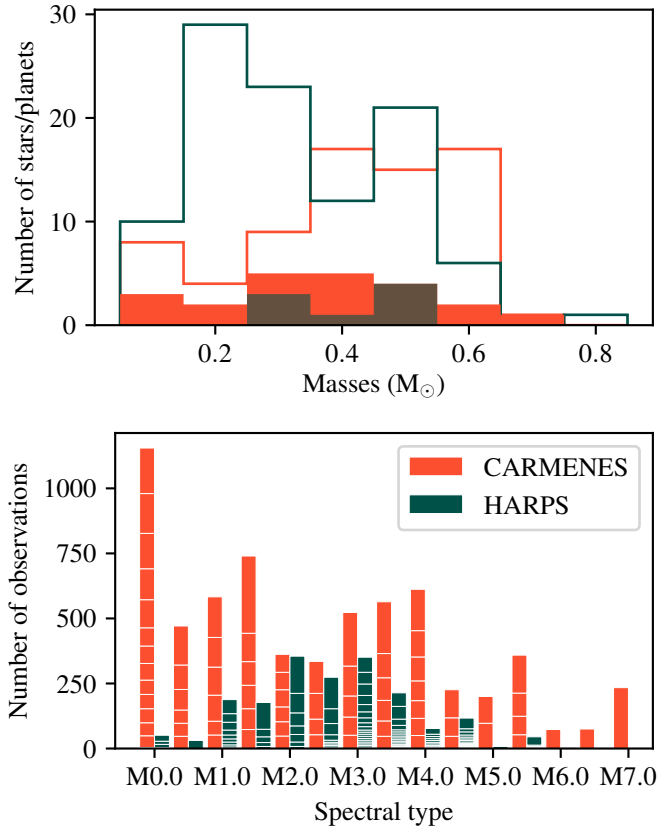


Fig. 10. Comparison of the CARMENES and the HARPS M dwarf surveys. *Top panel:* Stellar mass distributions of the CARMENES (this work; red) and HARPS (Bonfils et al. 2013; dark green) surveys. Open histograms depict all target stars (CARMENES: 71; HARPS: 102). Filled histograms depict stars with planets (CARMENES: 22; HARPS: 8). *Bottom panel:* Distribution of the number of spectra over spectral type in both surveys. HARPS spectral types are from Bonfils et al. (2013), and the number of RV values until 1 April 2009 is from Trifonov et al. (2020).

studies that analyze the *Kepler* M dwarf sample used subsamples of the one from Dressing & Charbonneau (2013). In this sample of ~ 4000 stars, about 20% are in the mass range of our lower stellar mass sample (786 stars) but only 1.5% are stars with less than $0.15 M_{\odot}$ (58 stars). The median mass of this large sample is $0.47 M_{\odot}$, which is higher than the median mass of the sample, which is investigated in this paper ($0.43 M_{\odot}$). Therefore, we need to keep in mind that if there is a trend in occurrence rate with stellar mass, the occurrence rates are not exactly comparable.

The comparison with our occurrence rates is also not straightforward for a second reason: transit surveys probe the planet radius, R_{pl} , whereas RV surveys probe $M_{\text{pl}} \sin i$. Mass and radius are related through bulk density, which can vary widely among small planets (e.g., Hatzes & Rauer 2015; Martínez-Rodríguez et al. 2019). As an extreme example, two super-Earths orbiting the same star (K2-106, TYC 608-458-1) were found to have densities 2.0 g cm^{-3} and 13.1 g cm^{-3} (Guenther et al. 2017). Similar contrasting densities are also measured, with the help of RV measurements, in multi-planetary systems discovered with the TESS, such as LTT 3780 b and c (Cloutier et al. 2020; Nowak et al. 2020). Therefore, the two parameters minimum mass and radius are not directly comparable. Nevertheless, we can compare the surveys on a statistical level with the mass-radius relations derived by Chen & Kipping (2017) for planets in

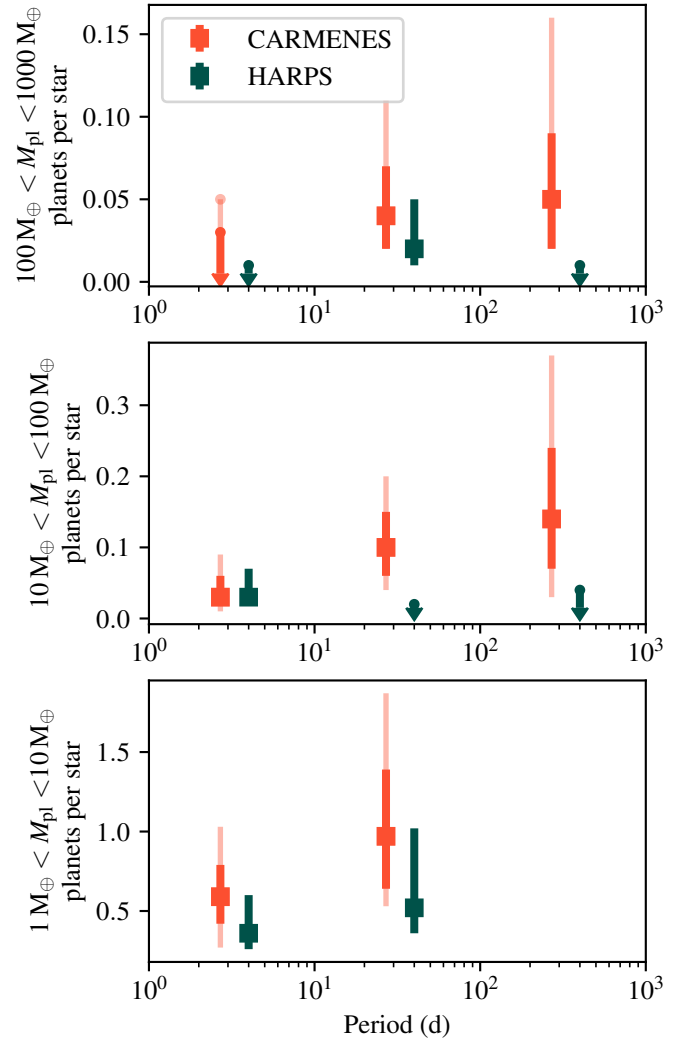


Fig. 11. CARMENES (red) and HARPS (dark green) planet occurrence rates as a function of planet orbital period for three different planet mass intervals. The CARMENES occurrence rates of the upper panel might suffer from a selection bias (see Sect. 4).

general or by Kanodia et al. (2019) for M dwarf planets. According to these mass-radius relations, our mass bin of $M_{\text{pl}} \sin i$ and $1 M_{\oplus} - 10 M_{\oplus}$ roughly corresponds to the radius interval $1 R_{\oplus} - 4 R_{\oplus}$ in transit surveys. In Fig. 12, we show a comparison of the low-mass or small planet occurrence rates in M dwarf samples as they are derived in various publications in the range of 1–100 d. Our values for the low-mass planet frequency are consistent with what is found in some publications of *Kepler* small planet occurrence rates, such as those by Mulders et al. (2015b) and Hsu et al. (2020). Furthermore, the results by Morton & Swift (2014), Dressing & Charbonneau (2015), Gaidos et al. (2016), and Hsu et al. (2020) indicate a ~ 1.5 times higher small-planet occurrence rate than ours. Yang et al. (2020) report 2.1 planets per star around M dwarfs but their period and mass range is much broader than ours ($0.4 - 20 R_{\oplus}$ and $P_{\text{pl}} < 400$ d). In a smaller radius and period range, their result could be consistent with ours. In Fig. 12, we plot two occurrence rates from Hsu et al. (2020), who work with two different distributions as priors for the planet size: (a) a Dirichlet prior over multiple radius bins per period range and (b) independent uniform priors for each bin.

Hardegree-Ullman et al. (2019) derive a small-planet occurrence rate as a function of spectral type (not shown in Fig. 12).

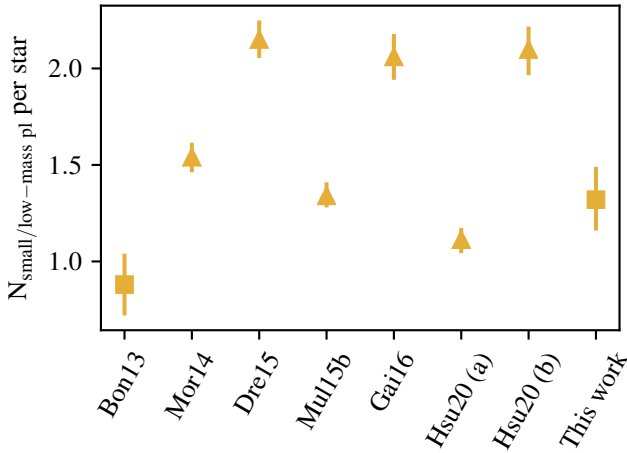


Fig. 12. Small or low-mass planet occurrence rate in M dwarfs from different surveys in the ranges of 1–100 d orbital period and $1 R_{\oplus}$ – $4 R_{\oplus}$ or $1 M_{\oplus}$ – $10 M_{\oplus}$. Error bars are derived from the square root of the planets in the sample in all cases to make them comparable. Triangles show the results from the *Kepler* transit surveys (Morton & Swift 2014; Dressing & Charbonneau 2015; Mulders et al. 2015b; Gaidos et al. 2016; Yang et al. 2020; Hsu et al. 2020) and squares the results from the HARPS and CARMENES RV surveys (Bonfils et al. 2013, and this work).

They find that the small-planet frequency increases toward later spectral types. Their limits are radii from $0.5 R_{\oplus}$ to $2.5 R_{\oplus}$ at periods of less than 10 d. Therefore, their absolute numbers are not comparable to ours. Nevertheless, we would expect to see the very same trend in our data. The lower panel of Fig. 7 shows exactly that behavior: in short orbits of up to 10 d, the low-mass planet occurrence rate of our low-mass stars is significantly higher than that of our more massive stars.

Mulders et al. (2015a) show that for various spectral types the small-planet frequency is lower at short orbital periods (in $\log P$ space). They obtain an occurrence rate of 27.9% for orbital periods of 1–10 d and 64.6% for orbital periods of 10–100 d. In a later publication based on more data from *Kepler*, they revised those occurrence rates to 35.7% and 98.3%, respectively (Mulders et al. 2015b). Therefore, their short-period occurrence rates are 2.32 or 2.75 times lower than those in the longer-period orbits. We see the same trend in our data if we consider the whole stellar sample, although not as prominent. Our short-period occurrence rate is 1.64 times lower than that for longer-period orbits. The low-mass planet occurrence around low-mass stars, on the other hand, shows a reverse or flat trend in period. We want to know if our results could still be consistent with a 2.32 times lower occurrence rate in the short-period bin. We thus counted the cumulative probability of such a simulation outcome, which is 0.36%. For this reason, we conclude that our results in the low stellar mass bin are not consistent with a drop in planet occurrence rate as high as 2.3 times. A reason for this could be the lower median stellar mass of our sample as compared to the sample in Mulders et al. (2015a). A more detailed study of planet occurrence rates for very low-mass stars will test if this result remains significant.

5. Conclusions

We calculate preliminary planet occurrence rates from a first subsample of 71 CARMENES GTO M dwarfs. The giant planet ($100 M_{\oplus} < M_{\text{pl}} \sin i < 1000 M_{\oplus}$) occurrence rate in our sample is $0.06^{+0.04}_{-0.03}\%$ for periods of up to 1000 d. We set an upper limit of

0.03 planets per star for hot Jupiters ($P < 10$ d). The most massive close-in planet that we detect has a mass of $21.4 M_{\oplus}$. Overall, the giant planet occurrence rate in our sample increases toward long periods, and it is lower than or equal to that around G-type stars. The analysis of the full 329 star sample of the CARMENES survey will show if there is a selection bias that could lead to an overestimation of the giant planet occurrence rate by up to a factor of five.

For intermediate-mass planets with minimum masses between $10 M_{\oplus}$ and $100 M_{\oplus}$, we similarly find an increase in the planet frequency toward long periods, in contrast to the results presented by Bonfils et al. (2013). The total occurrence rate is $0.18^{+0.07}_{-0.05}$ intermediate-mass planets per star.

Low-mass planets ($1 M_{\oplus} < M_{\text{pl}} \sin i < 10 M_{\oplus}$) are very abundant in our sample: We measure an occurrence rate of $1.32^{+0.33}_{-0.31}$ low-mass planets per star for periods of up to 100 d. This result is consistent with, or lower than, the results from the *Kepler* survey (see Fig. 12). It confirms an at least twice higher abundance of low-mass planets around M dwarfs as compared to G dwarfs (Mayor et al. 2011, Sect. 3.5). In a sample of late-type M dwarfs with stellar mass $M_{\star} < 0.34 M_{\odot}$, we find a very high low-mass planet occurrence rate in orbits shorter than 10 d, which is in agreement with results from the *Kepler* survey. Although from *Kepler* results the planet occurrence rate is expected to be lower in short-period orbits, our results imply that the low-mass planet occurrence rate in longer-period orbits is the same as or lower than in shorter-period orbits around our sample of low-mass stars.

We consolidate previous evidence for a high frequency of low-mass planets around the least massive stars, which poses constraints on the radial distribution and migration of planetary building blocks. Stellar mass-dependent planet formation models will have to explain the increased efficiency of turning these building blocks into planets in M dwarf systems. To this end, an investigation of our findings with the core accretion model by Burn et al. (2021) is already in progress (Schlecker et al., in prep.). This and future comparisons between observed with theoretically predicted trends will help to shed light on different planet formation conditions as a function of stellar host mass.

Acknowledgements. We thank the anonymous referee for many useful comments and suggestions that helped improving our paper. We thank M. Esposito for the explanation of his detection limit method and V. Wolthoff for useful insights in occurrence rate retrieval methods. This work was supported by the Thüringer Ministerium für Wirtschaft, Wissenschaft und Digitale Gesellschaft, and the Deutsche Forschungsgemeinschaft (DFG) under the DFG Research Unit FOR2544 “Blue Planets around Red Stars” (RE 2694/8-1) and the project GU 464/20-1. CARMENES is an instrument at the Centro Astronómico Hispano-Alemán (CAHA) at Calar Alto (Almería, Spain), operated jointly by the Junta de Andalucía and the Instituto de Astrofísica de Andalucía (CSIC). CARMENES was funded by the Max-Planck-Gesellschaft (MPG), the Consejo Superior de Investigaciones Científicas (CSIC), the Ministerio de Economía y Competitividad (MINECO) and the European Regional Development Fund (ERDF) through projects FICTS-2011-02, ICTS-2017-07-CAHA-4, and CAHA16-CE-3978, and the members of the CARMENES Consortium (Max-Planck-Institut für Astronomie, Instituto de Astrofísica de Andalucía, Landessternwarte Königstuhl, Institut de Ciències de l’Espai, Institut für Astrophysik Göttingen, Universidad Complutense de Madrid, Thüringer Landessternwarte Tautenburg, Instituto de Astrofísica de Canarias, Hamburger Sternwarte, Centro de Astrobiología and Centro Astronómico Hispano-Alemán), with additional contributions by the MINECO, the Deutsche Forschungsgemeinschaft through the Major Research Instrumentation Programme and Research Unit FOR2544 “Blue Planets around Red Stars”, the Klaus Tschira Stiftung, the states of Baden-Württemberg and Niedersachsen, and by the Junta de Andalucía. We acknowledge financial support from the Agencia Estatal de Investigación of the Ministerio de Ciencia, Innovación y Universidades and the ERDF through projects PID2019-109522GB-C51[4]/AEI/10.13039/501100011033 and the Centre of Excellence “Severo Ochoa” and “María de Maeztu” awards to the Instituto de Astrofísica de Canarias (SEV-2015-0548), Instituto de Astrofísica

de Andalucía (SEV-2017-0709), and Centro de Astrobiología (MDM-2017-0737), the Generalitat de Catalunya/CERCA programme, the DFG program SPP 1992 “Exploring the Diversity of Extrasolar Planets” (JE 701/5-1), and NASA (NNX17AG24G).

References

- Amado, P. J., Bauer, F. F., Rodríguez López, C., et al. 2021, *A&A*, **650**, A188
- Andrews, S. M., Rosenfeld, K. A., Kraus, A. L., & Wilner, D. J. 2013, *ApJ*, **771**, 129
- Ansdell, M., Williams, J. P., van der Marel, N., et al. 2016, *ApJ*, **828**, 46
- Astudillo-Defru, N., Forveille, T., Bonfils, X., et al. 2017, *A&A*, **602**, A88
- Bakos, G. A., Bayliss, D., Bento, J., et al. 2020, *AJ*, **159**, 267
- Barnes, J. R., Jeffers, S. V., & Jones, H. R. A. 2011, *MNRAS*, **412**, 1599
- Baroch, D., Morales, J. C., Ribas, I., et al. 2018, *A&A*, **619**, A32
- Bauer, F. F., Zechmeister, M., Kaminski, A., et al. 2020, *A&A*, **640**, A50
- Bayliss, D., Gillen, E., Eiglmüller, P., et al. 2018, *MNRAS*, **475**, 4467
- Bluhm, P., Luque, R., Espinoza, N., et al. 2020, *A&A*, **639**, A132
- Bonfils, X., Forveille, T., Delfosse, X., et al. 2005, *A&A*, **443**, L15
- Bonfils, X., Delfosse, X., Udry, S., et al. 2013, *A&A*, **549**, A109
- Borucki, W. J., Koch, D., Basri, G., et al. 2010, *Science*, **327**, 977
- Bryson, S., Kunimoto, M., Kopparapu, R. K., et al. 2021, *AJ*, **161**, 36
- Burn, R., Schlecker, M., Mordasini, C., et al. 2021, *A&A*, in press <https://doi.org/10.1051/0004-6361/202140390>
- Butler, R. P., Vogt, S. S., Marcy, G. W., et al. 2004, *ApJ*, **617**, 580
- Caballero, J. A., Cortés-Contreras, M., Alonso-Floriano, F. J., et al. 2016a, in 19th Cambridge Workshop on Cool Stars, Stellar Systems and the Sun (CS19), 148
- Caballero, J. A., Guàrdia, J., López del Fresno, M., et al. 2016b, in *Society of Photo-Optical Instrumentation Engineers (SPIE) Conference Series*, 9910, Observatory Operations: Strategies, Processes, and Systems VI, eds. A. B. Peck, R. L. Seaman, & C. R. Benn, 99100E
- Chen, J., & Kipping, D. 2017, *ApJ*, **834**, 17
- Cifuentes, C., Caballero, J. A., Cortés-Contreras, M., et al. 2020, *A&A*, **642**, A115
- Cloutier, R., Eastman, J. D., Rodríguez, J. E., et al. 2020, *AJ*, **160**, 3
- Cumming, A. 2004, *MNRAS*, **354**, 1165
- Cumming, A., Marcy, G. W., & Butler, R. P. 1999, *ApJ*, **526**, 890
- Cumming, A., Butler, R. P., Marcy, G. W., et al. 2008, *PASP*, **120**, 531
- Czesla, S., Schröter, S., Schneider, C. P., et al. 2019, *PyA: Python astronomy-related packages*
- Dreizler, S., Crossfield, I. J. M., Kossakowski, D., et al. 2020, *A&A*, **644**, A127
- Dressing, C. D., & Charbonneau, D. 2013, *ApJ*, **767**, 95
- Dressing, C. D., & Charbonneau, D. 2015, *ApJ*, **807**, 45
- Emsenhuber, A., Mordasini, C., Burn, R., et al. 2021, *A&A*, in press <https://doi.org/10.1051/0004-6361/202038553>
- Endl, M., Cochran, W. D., Kürster, M., et al. 2006, *ApJ*, **649**, 436
- Foreman-Mackey, D., Hogg, D. W., & Morton, T. D. 2014, *ApJ*, **795**, 64
- Gaidos, E., Mann, A. W., Kraus, A. L., & Ireland, M. 2016, *MNRAS*, **457**, 2877
- Gaudi, B. S. 2021, ArXiv e-prints [arXiv:2102.01715]
- Gillon, M., Triaud, A. H. M. J., Demory, B.-O., et al. 2017, *Nature*, **542**, 456
- González-Álvarez, E., Zapatero Osorio, M. R., Caballero, J. A., et al. 2020, *A&A*, **637**, A93
- Guenther, E. W., Barragán, O., Dai, F., et al. 2017, *A&A*, **608**, A93
- Hardegree-Ullman, K. K., Cushing, M. C., Muirhead, P. S., & Christiansen, J. L. 2019, *AJ*, **158**, 75
- Hartman, J. D., Bayliss, D., Brahm, R., et al. 2015, *AJ*, **149**, 166
- Hatzes, A. P. 2016, *A&A*, **585**, A144
- Hatzes, A. P., & Rauer, H. 2015, *ApJ*, **810**, L25
- Henry, T. J., Jao, W.-C., Subasavage, J. P., et al. 2006, *AJ*, **132**, 2360
- Henry, T. J., Jao, W.-C., Winters, J. G., et al. 2018, *AJ*, **155**, 265
- Howard, A. W., Marcy, G. W., Johnson, J. A., et al. 2010, *Science*, **330**, 653
- Howard, A. W., Marcy, G. W., Bryson, S. T., et al. 2012, *ApJS*, **201**, 15
- Hsu, D. C., Ford, E. B., & Terrien, R. 2020, *MNRAS*, **498**, 2249
- Ida, S., & Lin, D. N. C. 2010, *ApJ*, **719**, 810
- Jeffers, S. V., Barnes, J. R., Jones, H. R. A., et al. 2014, *MNRAS*, **438**, 2717
- Johnson, J. A., Gazak, J. Z., Apps, K., et al. 2012, *AJ*, **143**, 111
- Kaminski, A., Trifonov, T., Caballero, J. A., et al. 2018, *A&A*, **618**, A115
- Kanodia, S., Wolfgang, A., Stefansson, G. K., Ning, B., & Mahadevan, S. 2019, *ApJ*, **882**, 38
- Kemmer, J., Stock, S., Kossakowski, D., et al. 2020, *A&A*, **642**, A236
- Kipping, D. M. 2013, *MNRAS*, **434**, L51
- Lalitha, S., Baroch, D., Morales, J. C., et al. 2019, *A&A*, **627**, A116
- Luque, R., Nowak, G., Pallé, E., et al. 2018, *A&A*, **620**, A171
- Mann, A. W., Dupuy, T., Kraus, A. L., et al. 2019, *ApJ*, **871**, 63
- Marcy, G. W., Butler, R. P., Fischer, D., et al. 2001, *ApJ*, **556**, 296
- Martínez-Rodríguez, H., Caballero, J. A., Cifuentes, C., Piro, A. L., & Barnes, R. 2019, *ApJ*, **887**, 261
- Mayor, M., Marmier, M., Lovis, C., et al. 2011, ArXiv e-prints [arXiv:1109.2497]
- Meunier, N., Lagrange, A. M., & De Bondt, K. 2012, *A&A*, **545**, A87
- Moe, M., & Kratter, K. M. 2021, *MNRAS*, **507**, 3593
- Morales, J. C., Mustill, A. J., Ribas, I., et al. 2019, *Science*, **365**, 1441
- Mordasini, C., Alibert, Y., Benz, W., Klahr, H., & Henning, T. 2012a, *A&A*, **541**, A97
- Mordasini, C., Alibert, Y., Klahr, H., & Henning, T. 2012b, *A&A*, **547**, A111
- Morton, T. D., & Swift, J. 2014, *ApJ*, **791**, 10
- Mulders, G. D., Pascucci, I., & Apai, D. 2015a, *ApJ*, **798**, 112
- Mulders, G. D., Pascucci, I., & Apai, D. 2015b, *ApJ*, **814**, 130
- Nagel, E., Czesla, S., Schmitt, J. H. M. M., et al. 2019, *A&A*, **622**, A153
- Ndugu, N., Bitsch, B., & Jurua, E. 2018, *MNRAS*, **474**, 886
- Nowak, G., Luque, R., Parviainen, H., et al. 2020, *A&A*, **642**, A173
- Obermeier, C., Koppenhoefer, J., Saglia, R. P., et al. 2016, *A&A*, **587**, A49
- Pascucci, I., Testi, L., Herczeg, G. J., et al. 2016, *ApJ*, **831**, 125
- Quirrenbach, A., Amado, P. J., Caballero, J. A., et al. 2014, *Society of Photo-Optical Instrumentation Engineers (SPIE) Conference Series*, 9147, CARMENES instrument overview, 91471F
- Reiners, A., Ribas, I., Zechmeister, M., et al. 2018a, *A&A*, **609**, L5
- Reiners, A., Zechmeister, M., Caballero, J. A., et al. 2018b, *A&A*, **612**, A49
- Reylé, C., Jardine, K., Fouqué, P., et al. 2021, *A&A*, **650**, A201
- Ribas, I., Tuomi, M., Reiners, A., et al. 2018, *Nature*, **563**, 365
- Robertson, P., Mahadevan, S., Endl, M., & Roy, A. 2014, *Science*, **345**, 440
- Schlecker, M., Mordasini, C., Emsenhuber, A., et al. 2021a, *A&A*, in press <https://doi.org/10.1051/0004-6361/202038554>
- Schlecker, M., Pham, D., Burn, R., et al. 2021b, *A&A*, in press <https://doi.org/10.1051/0004-6361/202140551>
- Schöfer, P., Jeffers, S. V., Reiners, A., et al. 2019, *A&A*, **623**, A44
- Schweitzer, A., Passegger, V. M., Cifuentes, C., et al. 2019, *A&A*, **625**, A68
- Stock, S., Kemmer, J., Reffert, S., et al. 2020a, *A&A*, **636**, A119
- Stock, S., Nagel, E., Kemmer, J., et al. 2020b, *A&A*, **643**, A112
- Suárez Mascareño, A., Rebolo, R., González Hernández, J. I., & Esposito, M. 2017, *MNRAS*, **468**, 4772
- Tal-Or, L., Zechmeister, M., Reiners, A., et al. 2018, *A&A*, **614**, A122
- Tremaine, S., & Dong, S. 2012, *AJ*, **143**, 94
- Trifonov, T., Kürster, M., Zechmeister, M., et al. 2018, *A&A*, **609**, A117
- Trifonov, T., Tal-Or, L., Zechmeister, M., et al. 2020, *A&A*, **636**, A74
- Trifonov, T., Caballero, J. A., Morales, J. C., et al. 2021, *Science*, **371**, 1038
- Tychoniec, Ł., Tobin, J. J., Karska, A., et al. 2018, *ApJS*, **238**, 19
- Wittenmyer, R. A., Butler, R. P., Horner, J., et al. 2020, *MNRAS*, **491**, 5248
- Wright, J., Marcy, G., Howard, A., et al. 2012, *ApJ*, **753**, 160
- Wright, D. J., Wittenmyer, R. A., Tinney, C. G., Bentley, J. S., & Zhao, J. 2016, *ApJ*, **817**, L20
- Yang, J.-Y., Xie, J.-W., & Zhou, J.-L. 2020, *AJ*, **159**, 164
- Zechmeister, M., & Kürster, M. 2009, *A&A*, **496**, 577
- Zechmeister, M., Kürster, M., & Endl, M. 2009, *A&A*, **505**, 859
- Zechmeister, M., Reiners, A., Amado, P. J., et al. 2018, *A&A*, **609**, A12
- Zechmeister, M., Dreizler, S., Ribas, I., et al. 2019, *A&A*, **627**, A49

Appendix A: Long table

Table A.1. Output of the periodicity search program.

Karmn	Name	α (J2016)	δ (J2016)	M_* (M_\odot)	$N_{\text{obs,VIS}}$	P (d)	FAP (%)	Remark
J00051+457	GJ 2	1.3007478670	45.785915382	0.518	52	No signal
J00067-075	GJ 1002	1.676464124	-7.546212317	0.116	89	21.17	0.521	Unsolved
J00183+440	GX And	4.612667737	44.024729578	0.391	114	40.65	0.585	Rotation
J01025+716	Ross 318	15.658240193	71.678173532	0.488	115	43.39	<10 ⁻⁴	CaIRT
J01026+623	BD+61 195	15.668732123	62.34543864	0.515	80	9.33	0.01	Rotation
J01026+623	BD+61 195	15.668732123	62.34543864	0.515	80	18.9	0.315	CaIRT, H α
J01125-169	YZ Cet	18.133079241	-16.996243422	0.142	108	3.06	0.005	Planet
J01125-169	YZ Cet	18.133079241	-16.996243422	0.142	108	80.62	0.017	dLW
J01125-169	YZ Cet	18.133079241	-16.996243422	0.142	108	4.7	0.035	Planet
J02222+478	BD+47 612	35.562403121	47.88020753	0.551	47	28.23	0.007	CaIRT, dLW
J02362+068	BX Cet	39.071425223	6.877888387	0.262	50	No signal
J02442+255	VX Ari	41.068748746	25.521801507	0.357	51	No signal
J02530+168	Teegarden's Star	43.269144864	16.86490241	0.089	234	4.91	<10 ⁻⁴	Planet
J02530+168	Teegarden's Star	43.269144864	16.86490241	0.089	234	11.41	<10 ⁻⁴	Planet
J02530+168	Teegarden's Star	43.269144864	16.86490241	0.089	234	172.34	0.001	dLW
J03133+047	CD Cet	48.35301547	4.775188109	0.161	103	2.29	<10 ⁻⁴	Planet
J03133+047	CD Cet	48.35301547	4.775188109	0.161	103	67.91	0.344	Rotation
J03463+262	HD 23453	56.585773281	26.214660371	0.562	50	No signal
J04153-076	σ^2 Eri C	63.829970524	-7.670429685	0.284	47	1.8	<10 ⁻⁴	CRX
J04290+219	BD+21 652	67.250204922	21.923451047	0.650	150	12.53	0.005	Rotation
J04290+219	BD+21 652	67.250204922	21.923451047	0.650	150	25.07	0.004	CaIRT, dLW
J04290+219	BD+21 652	67.250204922	21.923451047	0.65	150	175.22	0.031	CRX
J04376+528	BD+52 857	69.422714035	52.89156892	0.578	119	16.3	0.193	CaIRT, dLW
J04376+528	BD+52 857	69.422714035	52.89156892	0.578	119	7.9	0.197	Unsolved
J04376+528	BD+52 857	69.422714035	52.89156892	0.578	119	422.79	0.219	Unsolved
J04588+498	BD+49 1280	74.711477815	49.848799932	0.589	55	8.97	0.008	Unsolved
J05314-036	HD 36395	82.867435093	-3.68623703	0.556	90	37.08	0.003	CaIRT, H α , dLW
J05314-036	HD 36395	82.867435093	-3.68623703	0.556	90	10000.0	<10 ⁻⁴	$P >$ time baseline/2
J06011+595	G 192-013	90.29510135819	59.593191709	0.257	79	83.39	0.07	dLW
J06011+595	G 192-013	90.29510135819	59.593191709	0.257	79	44.1	0.373	Unsolved
J06011+595	G 192-013	90.29510135819	59.593191709	0.257	79	21.52	0.663	Unsolved
J06103+821	GJ 226	92.584271112	82.101001876	0.415	57	10000.0	0.023	$P >$ time baseline/2
J06105-218	HD 42581 A	92.643599341	-21.867723301	0.528	51	2621.41	<10 ⁻⁴	$P >$ time baseline/2
J06371+175	HD 260655	99.291542865	17.566269572	0.456	55	No signal
J06548+332	Wolf 294	103.700249916	33.266463248	0.36	206	14.21	<10 ⁻⁴	Planet
J06548+332	Wolf 294	103.700249916	33.266463248	0.36	206	67.59	<10 ⁻⁴	Rotation
J06548+332	Wolf 294	103.700249916	33.266463248	0.36	206	119.48	<10 ⁻⁴	Rotation
J08413+594	LP 090-018	130.331661582	59.491836367	0.123	146	206.39	<10 ⁻⁴	Planet
J08413+594	LP 090-018	130.331661582	59.491836367	0.123	146	2236.05	<10 ⁻⁴	$P >$ time baseline/2
J08413+594	LP 090-018	130.331661582	59.491836367	0.123	146	39.3	0.038	Unsolved
J09143+526	HD 79210	138.583915757	52.684159157	0.586	70	16.32	<10 ⁻⁴	CaIRT, H α , dLW
J09143+526	HD 79210	138.583915757	52.684159157	0.586	70	1468.72	0.02	$P >$ time baseline/2
J09144+526	HD 79211	138.591672199	52.683521065	0.592	153	1432.22	<10 ⁻⁴	$P >$ time baseline/2
J09144+526	HD 79211	138.591672199	52.683521065	0.592	153	24.4	0.001	Planet
J09144+526	HD 79211	138.591672199	52.683521065	0.592	153	16.66	<10 ⁻⁴	CaIRT, H α , dLW
J09561+627	BD+63 869	149.033267235	62.785950488	0.574	67	18.66	<10 ⁻⁴	CaIRT, dLW
J09561+627	BD+63 869	149.033267235	62.785950488	0.574	67	8.93	0.028	Unsolved
J10122-037	AN Sex	153.072958611	-3.746713797	0.526	73	10.65	<10 ⁻⁴	Rotation
J10122-037	AN Sex	153.072958611	-3.746713797	0.526	73	21.4	0.006	CaIRT
J10289+008	BD+01 2447	157.228867166	0.837848462	0.426	67	305.89	0.017	Unsolved
J10482-113	LP 731-058	162.055102017	-11.342590886	0.117	75	1.52	0.07	Rotation
J10482-113	LP 731-058	162.055102017	-11.342590886	0.117	75	2.93	0.032	dLW
J10564+070	CN Leo	164.102166667	7.002194444	0.132	73	2.7	<10 ⁻⁴	CRX, dLW
J10584-107	LP 731-076	164.615773701	-10.775499854	0.208	45	4.62	<10 ⁻⁴	CRX
J11000+228	Ross 104	165.015742945	22.831741481	0.386	60	No signal
J11033+359	Lalande 21185	165.830959676	35.948653033	0.354	297	12.94	<10 ⁻⁴	Planet
J11033+359	Lalande 21185	165.830959676	35.948653033	0.354	297	1960.31	<10 ⁻⁴	$P >$ time baseline/2

Notes. Output of the periodicity search program of the 71 stars of the complete CARMENES subsample. Up to three signals with a periodogram FAP <1% are listed per star.

Table A.1. continued.

Karmn	Name	α (J2016)	δ (J2016)	M_{\star} (M_{\odot})	$N_{\text{obs,VIS}}$	P (d)	FAP (%)	Remark
J11054+435	BD+44 2051A	166.342583333	43.530972222	0.372	108	1043.71	0.001	$P >$ time baseline/2
J11110+304W	HD 97101 B	167.763593814	30.443921508	0.538	48	No signal
J11417+427	Ross 1003	175.432608072	42.751586224	0.354	76	41.28	$<10^{-4}$	Planet
J11417+427	Ross 1003	175.432608072	42.751586224	0.354	76	514.72	$<10^{-4}$	Planet
J11421+267	Ross 905	175.550536327	26.703066902	0.426	99	2.64	$<10^{-4}$	Planet
J11421+267	Ross 905	175.550536327	26.703066902	0.426	99	56.29	0.932	Unsolved
J11511+352	BD+36 2219	177.779128394	35.273104447	0.456	109	11.12	0.003	Rotation
J11511+352	BD+36 2219	177.779128394	35.273104447	0.456	109	25.5	0.52	Unsolved
J12123+544S	HD 238090	183.08863753	54.486153045	0.578	108	13.68	$<10^{-4}$	Planet
J12123+544S	HD 238090	183.08863753	54.486153045	0.578	108	107.28	0.455	Activity
J12312+086	BD+09 2636	187.813082661	8.808353196	0.55	50	No signal
J12479+097	Wolf 437	191.98153096	9.749418089	0.306	47	1.47	0.001	Planet
J13229+244	Ross 1020	200.733535753	24.463942534	0.272	92	3.02	$<10^{-4}$	Planet
J13229+244	Ross 1020	200.733535753	24.463942534	0.272	92	87.38	0.165	CRX, dLW
J14257+236W	BD+24 2733A	216.434869646	23.61227393	0.602	64	No signal
J14307-086	BD-07 3856	217.693284972	-8.647357533	0.63	94	249.07	0.353	Unsolved
J16167+672S	HD 147379	244.172568593	67.239204096	0.627	175	86.9	$<10^{-4}$	Planet
J16167+672S	HD 147379	244.172568593	67.239204096	0.627	175	361.2	$<10^{-4}$	CRX
J16167+672S	HD 147379	244.172568593	67.239204096	0.627	175	22.06	0.002	CaIRT, H α , dLW
J16303-126	V2306 Oph	247.574827573	-12.667686638	0.294	93	1.26	0.453	Planet
J16303-126	V2306 Oph	247.574827573	-12.667686638	0.294	93	17.88	0.001	Planet
J17303+055	BD+05 3409	262.594829884	5.547444738	0.537	54	33.77	0.605	CaIRT, H α , CRX, dLW
J17378+185	BD+18 3421	264.476487839	18.595950946	0.426	100	15.52	0.001	Planet
J17378+185	BD+18 3421	264.476487839	18.595950946	0.426	100	480.52	0.007	Activity
J17378+185	BD+18 3421	264.476487839	18.595950946	0.426	100	40.3	0.004	CaIRT, H α
J17578+046	Barnard's Star	269.448614358	4.737980766	0.172	199	311.25	0.001	Rotation
J18051-030	HD 165222	271.284034579	-3.032751785	0.45	53	No signal
J18174+483	TYC 3529-1437-1	274.354394178	48.367522828	0.587	69	16.04	0.324	Rotation
J18198-019	HD 168442	274.961836363	-1.93861271	0.593	136	No signal
J19169+051N	V1428 Aql	289.227732239	5.163161488	0.484	123	104.24	$<10^{-4}$	Planet
J19169+051N	V1428 Aql	289.227732239	5.163161488	0.484	123	174.48	0.001	Activity
J19169+051N	V1428 Aql	289.227732239	5.163161488	0.484	123	23.67	0.498	CRX
J19346+045	BD+04 4157	293.668264631	4.583853199	0.564	49	2.52	0.643	Unsolved
J20305+654	GJ 793	307.63811581	65.450778811	0.385	53	No signal
J20533+621	HD 199305	313.332456219	62.151065131	0.529	156	118.33	0.398	CRX
J20533+621	HD 199305	313.332456219	62.151065131	0.529	156	183.37	0.166	Unsolved
J21164+025	LSPM J2116+0234	319.114751335	2.580771066	0.43	81	14.45	$<10^{-4}$	Planet
J21164+025	LSPM J2116+0234	319.114751335	2.580771066	0.43	81	42.98	$<10^{-4}$	CaIRT
J21348+515	Wolf 926	323.712922362	51.53845905	0.446	70	26.34	0.332	Rotation
J21466+668	G 264-012	326.671959776	66.803848043	0.297	159	8.05	$<10^{-4}$	Planet
J21466+668	G 264-012	326.671959776	66.803848043	0.297	159	2.31	$<10^{-4}$	Planet
J21466+668	G 264-012	326.671959776	66.803848043	0.297	159	92.47	$<10^{-4}$	H α
J22021+014	BD+00 4810	330.540864624	1.399031119	0.548	79	10.96	0.041	Unsolved
J22057+656	G 264-018 A	331.435726824	65.649665641	0.482	91	123.74	$<10^{-4}$	CRX
J22096-046	BD-05 5715	332.422993791	-4.640831742	0.468	59	2380.57	$<10^{-4}$	$P >$ time baseline/2
J22096-046	BD-05 5715	332.422993791	-4.640831742	0.468	59	10000.0	0.015	$P >$ time baseline/2
J22114+409	1RXS J221124.3+410000	332.850163961	40.999928455	0.16	53	No signal
J22115+184	Ross 271	332.87688547	18.426973534	0.565	66	381.86	$<10^{-4}$	Unsolved
J22115+184	Ross 271	332.87688547	18.426973534	0.565	66	39.04	0.081	CaIRT, dLW
J22137-176	LP 819-052	333.432467485	-17.687062321	0.178	71	3.65	$<10^{-4}$	Planet
J22137-176	LP 819-052	333.432467485	-17.687062321	0.178	71	611.67	$<10^{-4}$	$P >$ time baseline/2
J22252+594	G 232-070	336.322145441	59.412502969	0.406	101	13.35	$<10^{-4}$	Planet
J22532-142	IL Aqr	343.323973712	-14.266595816	0.327	68	61.17	$<10^{-4}$	Planet
J22532-142	IL Aqr	343.323973712	-14.266595816	0.327	68	30.09	$<10^{-4}$	Planet
J23113+085	NLTT 56083	347.847583333	8.515583333	0.3	87	2225.31	$<10^{-4}$	$P >$ time baseline/2
J23113+085	NLTT 56083	347.847583333	8.515583333	0.3	87	141.09	$<10^{-4}$	Unsolved
J23216+172	LP 462-027	350.403614791	17.284434444	0.383	66	No signal
J23351-023	GJ 1286	353.796960795	-2.392682457	0.118	71	No signal
J23381-162	G 273-093	354.532727834	-16.236502771	0.374	55	No signal
J23419+441	HH And	355.479993699	44.170596761	0.143	97	178.74	$<10^{-4}$	Unsolved
J23419+441	HH And	355.479993699	44.170596761	0.143	97	93.21	0.543	dLW